



**KTH Aeronautical  
and Vehicle Engineering**

# Realistic Simulations of Delta Wing Aerodynamics Using Novel CFD Methods

Stefan Görtz

Royal Institute of Technology (KTH)  
Department of Aeronautical and Vehicle Engineering  
SE-100 44 Stockholm, Sweden

TRITA-AVE 2005:01  
ISSN 1651-7660  
ISBN 91-7283-938-4

Typsatt i  $\text{\LaTeX}$ .

TRITA-AVE 2005:01

ISSN 1651-7660

ISBN 91-7283-938-4

**Akademisk avhandling** som med tillstånd av Kungliga Tekniska högskolan i Stockholm framläggas till offentlig granskning för avläggande av teknologie doktorsexams tisdagen den 15 februari 2005 kl. 10.15 i Kollegiesalen, KTH, Valhallavägen 79, Stockholm.

© 2005 by Stefan Görtz

*The mere formulation of a problem is often far more essential than its solution, which may be merely a matter of mathematical skill.  
To raise new questions, new possibilities, to regard old problems from a new angle requires creative imagination and marks real advances in science.*

Albert Einstein



## Preface

This doctoral thesis is the result of work carried out at the Department of Aeronautical and Vehicle Engineering at the Royal Institute of Technology (KTH) and the Aeronautics Division (FFA) of the Swedish Defence Research Agency (FOI) in Stockholm, Sweden, between September 2000 and December 2004. The research has been partially funded by the National Program for Aeronautics Research (NFFP).

The thesis consists of an introduction to the research area, including some theoretical background, a summary of the most important results and some unpublished results, a CD-ROM with flow-field visualization videos, and the following appended papers<sup>1</sup>:

### Paper A

S. Görtz, A. Rizzi and K. Munukka, “Computational Study of Vortex Breakdown over Swept Delta Wings,” *AIAA Paper 99-3118*, 1999.

*Presented at the 17<sup>th</sup> AIAA Applied Aerodynamics Conference, Norfolk, June-July 1999.*

### Paper B

S. Görtz and A. Rizzi, “Computing the High-Alpha Aerodynamics of Delta Wings - Evaluation and Analysis,” *AIAA Paper 01-0115*, 2001.

*Presented at the 39<sup>th</sup> AIAA Aerospace Sciences Meeting & Exhibit, Reno, Jan. 2001.*

### Paper C

S. Görtz, “Time-accurate Euler Simulations of a Full-Span Delta Wing at High Incidence,” *AIAA Paper 03-4304*, 2003.

*Invited session paper, presented at the 21<sup>st</sup> AIAA Applied Aerodynamics Conference, Orlando, June 2003.*

### Paper D

S. Görtz, “Detached-Eddy Simulations of a Full-Span Delta Wing at High Incidence,” *AIAA Paper 03-4216*, 2003.

*Invited session paper, presented at the 21<sup>st</sup> AIAA Applied Aerodynamics Conference, Orlando, June 2003.*

---

<sup>1</sup>The papers are reset to comply with the present thesis format, and some minor corrections have been made.

**Paper E**

S. Görtz and A. Jirásek, "Steady and Unsteady CFD Analysis of the F-16XL-1 at Flight-Reynolds Numbers and Comparison to Flight Test Data," in *Understanding and Modelling Vortical Flows to Improve the Technology Readiness Level for Military Aircraft*, NATO RTO Technical Report, AVT-113, to appear in 2006.

**Paper F**

S. Görtz and E. Sundström, "Virtual Reality Environment for Visualization of Unsteady Three-Dimensional CFD Data," *Proceedings ECCOMAS 2004*, 2004.

*Presented at the European Congress on Computational Methods in Applied Sciences and Engineering, ECCOMAS 2004, Jyväskylä, Finland, July, 2004.*

**Paper G**

S. Görtz and J. Möller, "Recursive Projection Method for Efficient Unsteady CFD Simulations," *Proceedings ECCOMAS 2004*, 2004.

*Presented at the mini-symposium on Virtual Reality at the European Congress on Computational Methods in Applied Sciences and Engineering, ECCOMAS 2004, Jyväskylä, Finland, July, 2004.*

**Paper H**

S. Görtz and J. Möller, "Evaluations of the Recursive Projection Method for Efficient Turbulent Unsteady CFD Simulations," *ICAS Paper 2004-2.1.1*, 2004.

*Presented at the 24<sup>th</sup> Congress of the International Council of the Aeronautical Sciences (ICAS), Yokohama, Japan, Aug.-Sept. 2004.*

*This paper received the ICAS John McCarthy Award for Best Student Paper.*

Relevant publications not included in this thesis:

**Paper I**

A. Rizzi, S. Görtz and Y. Le Moigne, "Aspects of the Simulation of Vortex Flows over Delta Wings," in *Frontiers of Computational Fluid Dynamics – 2000*, World Scientific Publishing Company, June 2000.

## Paper J

S. Görtz, “Unsteady Euler and Detached-Eddy Simulations of Full-Span ONERA 70° Delta Wing,” in *Validation and Verification of CFD and Analytical Solutions for the Vortical Flow over Slender Delta Wings at High Incidence*, NATO RTO TR-084, 2005.

## Paper K

S. Görtz, “Unsteady Euler and Detached-Eddy Simulations of Vortex Breakdown over a Full-Span Delta Wing,” *Proceedings ECCOMAS 2004*, 2004.

*Invited Special Technological Session paper, presented at the European Congress on Computational Methods in Applied Sciences and Engineering, ECCOMAS 2004, Jyväskylä, Finland, July, 2004.*

## Division of Work between Authors

### Paper A

Munukka generated the numerical grids and wrote the paragraph on the results on the EC grid. Görtz wrote the rest of the paper, performed the numerical calculations and extracted the engineering data from the flow solver output. Rizzi guided the work and contributed to the paper with valuable comments and revisions.

### Paper B

Görtz generated the numerical grids, performed the numerical analysis and wrote the paper. Rizzi supervised the work and contributed with suggestions and valuable comments.

### Paper E

Jirásek helped to develop the best practices for computing the flow around the F-16XL-1 using the Edge CFD code.

### Paper F

Görtz initiated and supervised the work, performed the numerical calculations and wrote the paper, based on a report by Sundström. Sundström set up the VR environment and performed the visualization in the VR Cube.

### Paper G

Möller implemented RPM into Matlab. Görtz linked the Matlab implementatio to the Edge code, modified Edge to update the boundary conditions and generated the grid. The simulations and the write-up are joint work.

**Paper H**

Görtz extended the Matlab implementation of RPM to one- and two-equation turbulent models, modified Edge to update the turbulence quantities and generated the grid. The simulations and the write-up are joint work.

## Abstract

The overall goal of the research presented in this thesis is to extend the physical understanding of the unsteady external aerodynamics associated with highly maneuverable delta-wing aircraft by using and developing novel, more efficient computational fluid dynamics (CFD) tools. More specific, the main purpose is to simulate and better understand the basic fluid phenomena, such as vortex breakdown, that limit the performance of delta-wing aircraft. The problem is approached by going from the most simple aircraft configuration – a pure delta wing – to more complex configurations. As the flow computations of delta wings at high angle of attack have a variety of unusual aspects that make accurate predictions challenging, best practices for the CFD codes used are developed and documented so as to raise their technology readiness level when applied to this class of flows.

Initially, emphasis is put on subsonic steady-state CFD simulations of stand-alone delta wings to keep the phenomenon of vortex breakdown as clean as possible. For half-span models it is established that the essential characteristics of vortex breakdown are captured by a structured CFD code. The influence of viscosity on vortex breakdown is studied and numerical results for the aerodynamic coefficients, the surface pressure distribution and breakdown locations are compared to experimental data where possible.

In a second step, structured grid generation issues, numerical aspects of the simulation of this nonlinear type of flow and the interaction of a forebody with a delta wing are explored.

Then, on an increasing level of complexity, time-accurate numerical studies are performed to resolve the unsteady flow field over half and full-span, stationary delta wings at high angle of attack. Both Euler and Detached Eddy Simulations (DES) are performed to predict the streamwise oscillations of the vortex breakdown location about some mean position, asymmetry in the breakdown location due to the interaction between the left and right vortices, as well as the rotation of the spiral structure downstream of breakdown in a time-accurate manner. The computed flow-field solutions are visualized and analyzed in a virtual-reality environment.

Ultimately, steady-state and time-dependent simulations of a full-scale fighter-type aircraft configuration in steady flight are performed using the advanced turbulence models and the detached-eddy simulation capability of an edge-based, unstructured flow solver. The computed results are compared to flight-test data.

The thesis also addresses algorithmic efficiency and presents a novel implicit-explicit algorithm, the Recursive Projection Method (RPM), for computations of both steady and unsteady flows. It is demonstrated that RPM can accelerate such computations by up to 2.5 times.

**Keywords:** CFD, aerodynamics, flow physics, steady, unsteady, delta wing, vortical flow, vortex breakdown, vortex interactions, grid generation, grid refinement, time-accurate simulation, detached-eddy simulation, visualization, virtual reality, co-processing, algorithmic efficiency, recursive projection method.



## Contents

	Page
<b>Preface</b>	<b>i</b>
<b>Abstract</b>	<b>v</b>
<b>Introduction</b>	<b>1</b>
1. Background . . . . .	1
1.1. Computational Challenges in Delta-Wing Flow Predictions . . . . .	5
2. Scope of the Thesis . . . . .	6
2.1. Thesis Outline . . . . .	7
3. Delta Wings Aerodynamics . . . . .	8
3.1. Fundamentals . . . . .	8
3.2. Vortex Breakdown . . . . .	10
3.3. Previous Numerical Studies . . . . .	15
4. Computational Approach . . . . .	21
4.1. The Structured Navier-Stokes Multi Block Code NSMB . . . . .	21
4.2. The Unstructured Flow Solver Edge . . . . .	22
4.3. The Recursive Projection Method . . . . .	23
5. Pre- and Postprocessing . . . . .	31
5.1. Preprocessing . . . . .	31
5.2. Scientific Visualization . . . . .	33
5.3. Co-Processing Visualization with pV3 . . . . .	37
6. Summary of Appended Papers . . . . .	41
<b>Conclusions</b>	<b>53</b>
<b>Acknowledgements</b>	<b>55</b>
<b>References</b>	<b>57</b>
<b>Flow-Field Visualization Videos</b>	<b>65</b>
<b>Appended Papers A-H</b>	<b>69</b>



## List of Figures

Figure	Page
1 Delta-wing configurations . . . . .	1
2 Examples of aircraft with delta-wings under development . . . . .	2
3 NASA F-18 HARV smoke flow visualization . . . . .	3
4 NASA F-18 HARV forebody vortex flow visualization . . . . .	4
5 Schematic of the subsonic flow field over a delta wing . . . . .	8
6 Sketches of leading-edge vortex flow above delta wing . . . . .	9
7 Spiral and bubble-type vortex breakdown over a delta wing . . . . .	11
8 Stages of spiral breakdown . . . . .	12
9 Symmetric and asymmetric vortex breakdown . . . . .	14
10 Secondary vortex system associated with 'whorl' skin friction pattern	15
11 Schematic of a primary grid and its dual grid . . . . .	23
12 Dominant Eigenvalues captured by RPM . . . . .	25
13 RPM algorithm in pseudocode . . . . .	28
14 Schematic diagram of the Edge-Matlab implementation of RPM . . .	29
15 Flowchart of file exchange between Edge and Matlab . . . . .	29
16 Preprocessing steps required to create database for flow solver . . .	32
17 Data storage and visualization approach . . . . .	34
18 The three parts of pV3 . . . . .	37
19 Screenshot of pV3 Server . . . . .	38
20 Co-processing visualization tool . . . . .	39
21 Parallel co-processing visualization of CFD data with pV3 . . . . .	40
22 Computed vortex breakdown locations compared to experimental data	41
23 Vortex interaction over generic delta-wing/body compared . . . . .	43
24 Vortex breakdown and interaction over generic delta wing-body model	44
25 Computed skin friction lines on wing-body model . . . . .	44
26 Computed skin friction lines on cropped delta wing . . . . .	45
27 Normal force coefficient vs. time for different angles of attack . . . . .	46
28 Snap shots of time-dependent particles at different instances in time .	47
29 Computed and measured longitudinal velocity component . . . . .	48
30 New tetrahedral cells generated by AMR . . . . .	49
31 Flow over delta wing visualized in virtual-reality environment . . . . .	50
32 Comparison between the native Edge iteration scheme and RPM . . . .	51
33 Comparison between RPM restart and restart/update approach . . . . .	52



## Introduction

### 1. Background

Much of the past and present research and development efforts in aerodynamics are devoted to investigations of the flow phenomena which are accentuated as the angles of attack of complex configurations increase [1]. A relative new tool in the exploration of this flow regime is Computational Fluid Dynamics (CFD). CFD is the science of producing numerical solutions to a system of partial differential equations which describe fluid flow. CFD is done by discrete methods and the purpose is to better understand qualitatively and quantitatively physical phenomena in the flow which then is often used to improve upon engineering design [2]. Nowadays, CFD is considered to be an important supplement to classical wind tunnel experiments and plays an important role in modern high performance aircraft design and development [3, 4]. CFD simulations of the vortical flow over delta wings, in particular, have been and are of major interest because of the large number of airplanes (manned or unmanned), which generate these flows during flight. Some examples include Saab's JAS 39 "Gripen", shown in Fig. 1, Eurofighter, Dassault's Mirage 2000, Lockheed Martin's F-22 "Raptor", the Space Shuttle and Concorde.



Figure 1: Delta-wing configurations: Saab JAS-39 "Gripen" and Saab/Dassault UCAV (artists impression)

The same type of flow phenomena is also found in the new generation of unmanned aerial vehicles (UAV) and unmanned combat aerial vehicles (UCAV), such as the kite-shaped X-47A, a tailless naval UCAV built by Northrop Grumman. UCAVs seek to combine stealth technology with the lower cost and reduced risk of unmanned aircraft. Such changes in military requirements have resulted in a need to understand better the aircraft characteristics before committing to full-scale production. The stealth require-

ments for such prospective air vehicles may reduce the need for maneuverability, but their design, combining moderate to high sweep angles, sharp edges to lifting surfaces and bodies (e.g. chines), and novel control systems, will be associated with complex vortical flows and interaction effects at much lower angles of incidence than is the case for conventional fighter aircraft [5, 6].

Predicting and understanding vortical flows with the help of CFD will also be important for future air-vehicle concepts such as the European UCAV under development by Saab and Dassault, seen in Fig. 1, the Supersonic Transport (SST) by the Japanese Aerospace Exploration Agency (JAXA), shown in Fig. 2(a), the Gulfstream Quiet Supersonic Jet (QSJ) design, Fig. 2(b), Dassault's supersonic business jet Falcon SST, Fig. 2(c), or the “Flying Innovative Low-observable Unmanned Research vehicle” (FILUR), Fig. 2(d), which is currently being developed by Saab for the Swedish Defense Administration (FMV) and scheduled to perform its first autonomous flight in 2005.



(a) Next Generation Supersonic Transport (JAXA)



(b) Gulfstream Quiet Supersonic Jet (QSJ)



(c) Dassault supersonic business jet Falcon SST



(d) Saab low-signature UAV demonstrator FILUR

Figure 2: Examples of aircraft with delta-wing planforms currently under development (artist impressions)

While the historical knowledge of vortex flows is well established, it is dangerous to predict all the important flow features for such new configurations based on geometric similarities with an existing configuration [5]. Instead, such unconventional wing planforms require high fidelity CFD to predict their high-alpha aerodynamics.

All aircraft described above have in common that at moderate to high angles of attack a complex interaction of boundary layer separation and transition causes the flow to separate from the wing leading edges, forebodies, strakes, and leading-edge extensions, and roll up to form free vortices. The strength of the lift-enhancing wing

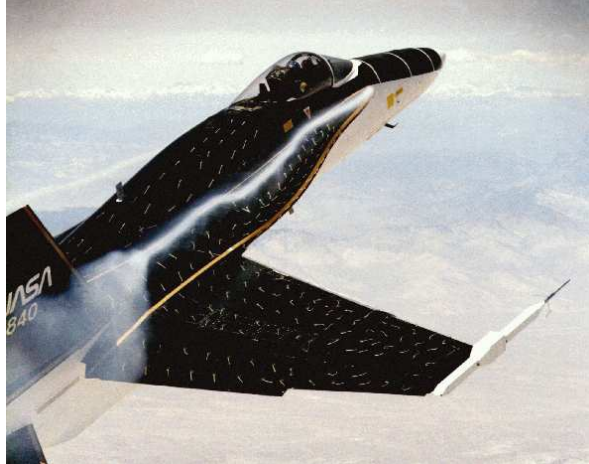


Figure 3: NASA F-18 HARV smoke flow visualization at 20°angle of attack. The smoke is injected into the flow at the apex of the strake and is confined in the compact strake vortex. The broadening of the smoke tube upstream of the twin tail indicates vortex breakdown.

vortices increases with angle of attack until a sudden disorganization occurs. This phenomenon, which is known as vortex breakdown or vortex burst, leads to rapid changes in the forces and moments experienced by the vehicle and hence to unexpected aerodynamic instability. At the same time, the vortices may degrade control surface effectiveness, or they may interact with each other, with shock waves, or directly with the vehicle structure causing catastrophic failure. Figure 3, e.g., shows the interaction of the burst strake vortices of NASA’s F-18 High Angle of Attack Research Vehicle (HARV) with the twin tail. This interaction occurs at moderate angles of attack and the resulting unsteady flow is known to cause tail buffet, which can lead to structural fatigue of the aft control surfaces or the entire tail assembly [7, 8]. The interaction between the forebody vortices and the burst strake vortices over the same vehicle at 42°angle of attack is shown in Fig. 4. This “weak interaction” [9] can lead to wing rock [10].

Conversely, if large scale, unsteady nonlinear vortex dynamics could be predicted accurately with confidence, control-system design could be improved and flight simulators could be made more representative [6]. Furthermore, such flows could be exploited to improve the vehicle performance. Vortical flows are therefore important for the performance, control, safety, and in-service costs of current and future air vehicles. The need to understand and predict such flows with confidence has never been greater. Numerical modeling, i.e. CFD, is the tool that has great potential to add in this quest.

Since the mid-sixties, the development of CFD methods to compute flow about a given geometry has progressed at a phenomenal pace, fueled by the tremendous growth in the speed and memory of computers and impressive advances in numerical



Figure 4: NASA F-18 HARV forebody vortex flow visualization at  $42^\circ$  angle of attack. The forebody vortex is seen to interact and merge with the burst strake vortex.

algorithms to solve the fluid-dynamic equations [3]. CFD methods for vortex-flow simulations can be broadly categorized into lower-order methods (based on potential-flow equations), inviscid Euler methods, and viscous Navier-Stokes methods [11]. The lower-order methods are widely accepted because of their rapid turnaround and low levels of labor and computer resources. But they do not offer the required level of fidelity because their simple physics model do not capture the nonlinear aerodynamic effects inherent to vortical flows. Euler and Navier-Stokes methods have demonstrated their ability of modeling vortex flows [12], but require tremendous computing and labor resources.

To the present day, most CFD studies of vortical flow have been limited to steady-state simulations. Of greater interest to the aircraft designer are perhaps the characteristics of such aerodynamic structures evolving in time [13], stimulating the demand for unsteady, or time-accurate, flow simulations, which may become the key technology for developing innovative configurations. Today, however, CFD must be considered as an experimental technique when applied to unsteady effects and must be supported by experiments for essentially all such problems, except for a few flows that are accessible to DNS with unambiguous boundary conditions [14]. Further development is needed before the accuracy and reliability of unsteady CFD techniques is sufficient for industrial applications, which currently rely on lower-level linear potential methods [3]. The unsteady CFD methods have also been rather ineffective to date in supplying unsteady aerodynamics data in a timely and cost-effective fashion. At least one or two orders of magnitude in computational time are required before unsteady CFD can support the development of new aerodynamic concepts.

Even when using high-fidelity methods, good results are obtained only with properly validated computer codes. Therefore, one key item for the aircraft designer is to have available CFD codes for which the Technology Readiness Level, i.e. confidence in the codes, has been increased [15]. When this has been accomplished, through comparison with model or flight-data at subsonic and transonic speeds in which the

flow field features vortices and/or shocks, an improved understanding and prediction of aircraft characteristics before fabrication will be possible. This translates into reduction of project risk and an enhanced analysis of system performance prior to flight. Moreover, it will also lead to tools, which can be applied to aid in the understanding of unexpected flight behavior that can occur during flight test.

### 1.1. Computational Challenges in Delta-Wing Flow Predictions

Aircraft aerodynamics have been predicted using computational fluid dynamics for a number of years. While viscous flow computations for cruise conditions have become commonplace, the non-linear effects that take place at high angles of attack are much more difficult to predict. A variety of difficulties arise when performing these computations, including challenges in properly modeling turbulence and transition for vortical and massively separated flows, the need to use appropriate numerical algorithms if flow asymmetry is possible, and the difficulties in creating grids that allow for accurate simulation of the flowfield [16]. Some of the other computational challenges in simulations of the flow over delta wings at high angle of attack are summarized in [5, 6] and are repeated below in no specific order:

- Computational methods for the prediction of interacting vortex flows are not yet fully proven.
- Tools to allow for the rapid computation of vortex flows about complex configurations are still at the research stage.
- Modeling the onset of vortex flow from boundary-layer separation on smooth surfaces is difficult.
- Prediction of vortex breakdown for complex vehicle configurations is challenging.
- Scale, compressibility and unsteady effects (such as asymmetry in the vortex breakdown location and its streamwise oscillation) need to be addressed.
- Vortex interaction effects need more attention across disciplines.
- Accurate predictions of the strength and position of the primary vortex core require an adequate grid and an adequate turbulence model, because massively separated flows defeat conventional turbulence models.
- Refinement studies should be undertaken to demonstrate grid convergence.

The ultimate challenge is the time-accurate CFD simulation of a full aircraft configuration at high angle of attack and flight Reynolds numbers using state-of-the-art turbulence modeling.

## 2. Scope of the Thesis

The overview presented above has outlined the complexity of vortical flows around high-performance delta-wing aircraft and the importance of enhancing the necessary understanding through the use of CFD. The present thesis addresses several of the topics highlighted in the overview and some of the computational challenges. The aim is to advance the physical understanding of the fundamental fluid mechanics associated with highly manoeuvrable aircraft by performing realistic CFD simulations. Realistic simulations are very demanding in terms of modeling accuracy, model fidelity and method/algorithmic efficiency. This motivates the use and development of novel CFD methods.

Initially, the problem is approached by studying simplified geometries, such as flat-plate delta wings and delta-wing/body models, that exhibit the vortical flow complexity associated with full aircraft configurations. The emphasis is on the numerical investigation of vortex breakdown at stationary angles of attack. For this purpose, the structured Navier-Stokes Multi-Block (NSMB) flow solver is used to compute steady and unsteady inviscid, laminar, and fully turbulent solutions to the Euler and Navier-Stokes equations for the flow over semi and full-span delta wings and a generic delta-wing/body model.

The larger values of  $\alpha$  required for the appearance of vortex breakdown tend to be associated with maneuvering rather than cruising flight, i.e. with changing rather than constant angle of attack. The study of the fundamental phenomenon, however, begins with stationary wings, because a maneuver may add further complexity to the aerodynamics (such as “dynamic overshoot,” or hysteresis). Furthermore, because of present CPU limitations, maneuver simulations have to be performed using either time steps that exceed the smallest physical time scales involved by orders of magnitude and/or coarse numerical grids. In both cases, the simulations are suitable for predicting global effects (aerodynamic forces and moments) rather than details of the flow field, compare e.g. [17]. Thus, before one can hope to predict complex maneuver aerodynamics including vortex breakdown consistently to the required accuracy, a capability for predicting the stationary flow field at high incidence must first be developed and demonstrated [6]. Finally, high angles of attack are also associated with the quasi-stationary flight of high-performance aircraft at takeoff and landing attitudes. Ensuring that a new design does not exhibit any unfavorable flying characteristics during these critical phases of flight through modeling and simulation of the high-alpha aerodynamics prior to first flight will greatly reduce the risk of any such project.

One new and important aspect is the demonstration/clarification/validation of time-accurate simulations of unsteady effects at high alpha (e.g. breakdown unsteadiness). Because such a simulation involves flows with multiple time scales, the time step size must be understood and selected for the accurate resolution of the essential flow features evolving on the different time scales. A good physical understanding for unsteady flow on slender (delta) wings and bodies is of the utmost importance for the study of agile aircraft and aircraft manoeuvres, and an accurate and efficient computational method can be an indispensable tool to the applied aerodynamicist in building up his physical insight and understanding of the problems and his engineering know-how. Typical related flow/flight-dynamics phenomena are hysteresis effects

and wing rock. Also, non-linear aerodynamic damping data will be an essential output of a computational method for unsteady external aerodynamics.

In addition to accuracy, computational efficiency is of paramount importance for unsteady numerical simulations because as the governing equations increase in complexity (viscosity, turbulence, etc.), the cost in terms of money and time of running the code determines whether it ultimately is useful as an engineering tool. The thesis addresses this problem by presenting a novel algorithm for unsteady CFD simulations.

This novel algorithm and other recent advances in numerical simulation capabilities have enabled the generation of very large amounts of data. There is a need to handle, store, integrate, and analyze these large data sets. It has also become difficult to extract synthetic or phenomenological information from these large quantities of detailed flow data and novel post-processing techniques must be applied to obtain the benefits of these superior tools. This thesis discusses some novel post- and co-processing methods and techniques that allow the extraction of physical characteristics of the flow over delta wings from sets of data that represent spatial or temporal distributions.

Finally, on an increasing level of complexity, a full aircraft configuration is investigated using the advanced turbulence models and the Detached-Eddy Simulation capability of Edge, a CFD code for unstructured grids. This is an important step towards realistic simulations of delta-wing configurations.

## 2.1. Thesis Outline

The thesis is divided into two main parts. In the first part, the reader is introduced to the aerodynamics of delta wings in more detail, followed by a review of previous experimental and numerical studies on high-alpha aerodynamics and vortex breakdown. Next is a chapter on the use and development of computational methods, followed by a discussion of visualization and post-processing techniques with an emphasis on visualization of unsteady data. Finally, the main results are summarized.

The second part of the thesis consists of the appended papers. Paper A is concerned with steady-state computations of vortex breakdown over half-span 70° delta wings. The emphasis is on mapping out the area of research and on comparing the predictive capability of different physical models. Paper B addresses several numerical and grid-generation aspects of the steady-state simulation of a delta wing and of the nonlinear vortex-vortex interactions over a generic delta-wing/body configuration. The third and fourth paper, Papers C and D, deal with time-accurate Euler and Detached-Eddy Simulations of vortex breakdown over a full-span delta wing. Here, the aim is to overcome the limitations of assuming symmetric steady-state behavior for a truly asymmetric and unsteady flow phenomenon. Paper E presents steady and unsteady computations of a full-scale delta-wing aircraft at three different flight Reynolds-Mach numbers combinations. The results reported in Papers C and D are visualized and analyzed in a virtual reality environment in Paper F. Finally, Papers G and H deal with improving the algorithmic efficiency of the CFD code used in the previous papers to pave the way for more wide-spread adoption of unsteady CFD in aircraft design and analysis.

### 3. Delta Wings Aerodynamics

#### 3.1. Fundamentals

The subsonic flow over delta wings with leading-edge separation has been described extensively in the literature and the knowledge of the flow topology is well established. It is sketched for a sharp-edged delta wing at angle of attack in Fig. 5.

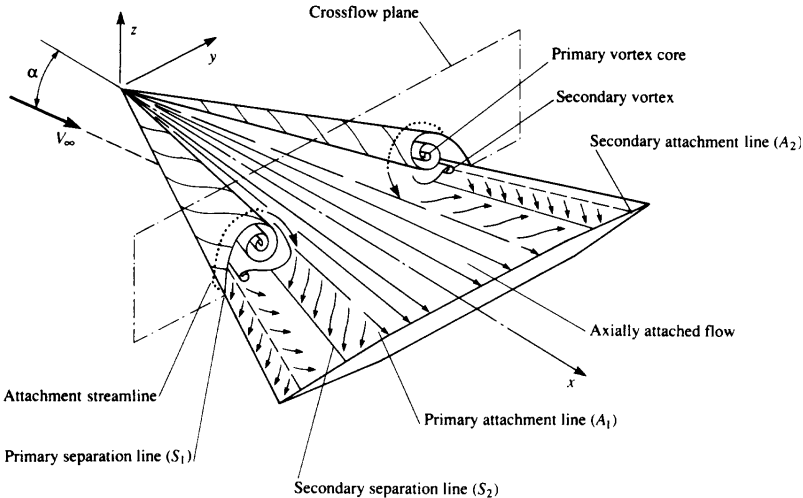


Figure 5: Schematic of the subsonic flow field over the top of a delta wing at angle of attack [18]

The dominant aspect of this flow are the two vortical structures that will form on wings with leading-edge sweep angles greater than  $45^\circ$ . At moderate to high angles of attack two dividing streamlines are formed on the lower surface of the wing, similar to the forward stagnation point in two-dimensional flow. Flow inboard of this dividing streamline just travels downstream, swept along by the streamwise component of velocity. The flow outboard the dividing streamline in the vicinity of the leading edge travels out and tries to curl around the leading edge to the upper surface. The flow separates when encountering the sharp leading edge (a geometrical singularity, the so-called primary separation line denoted  $S_1$  in Fig. 5) and, together with the boundary layer departing from the lee-side of the wing, forms a free shear layer, which springs into the outer non-dissipative flow. Under the influence of the vorticity contained within it, the free shear layer rolls up in a spiral fashion to form the fairly compact, steady primary vortex. It features a viscous core, with the vortex flow around it being essentially inviscid. The primary vortex remains embedded within the shear layer. It is continually fed with vorticity along the entire length of the leading edge of the wing. The vorticity is transported through the free shear layer to the vortex core, which is increasing in strength as well as in cross-sectional dimension in the downstream direction. A second stream surface or vortex sheet, lying above the primary vortex, loops

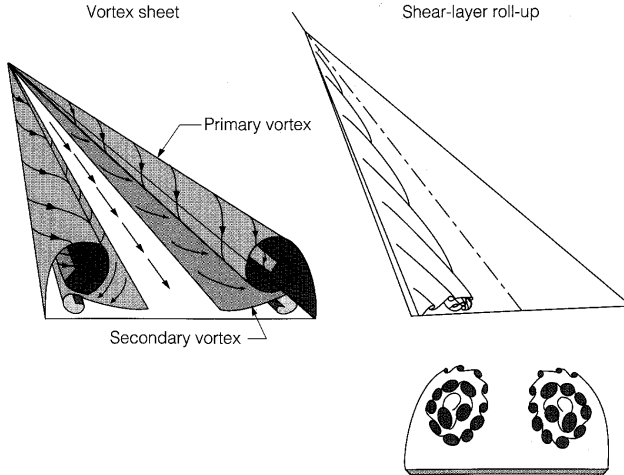


Figure 6: Sketches of leading-edge vortex flow above delta wing represented as vortex sheet (left) or instability vortices in separated shear layer (right) [19]

above the wing and reattaches along the primary attachment line  $A_1$ . The streamlines on the vortex sheet follow helical paths. The surface streamlines flow away from attachment lines, whereas they flow towards separation lines and lift off the surface along these lines. Inboard of the primary attachment lines  $A_1$ , the surface streamlines are attached and the flow downstream is undisturbed along a series of straight lines emanating from the apex of the wing. Outboard of the primary attachment lines, the flow entrained in the primary vortex moves outward beneath the primary vortex core towards the leading edge. It can separate near the wing surface at  $S_2$  due to the adverse pressure gradient the flow encounters in the spanwise direction. This separated flow may then form an oppositely rotating secondary vortex, which tends to move the primary vortex inboard and away from the upper surface of the wing. In low-speed flows the secondary separation location is found to be Reynolds number dependent. The secondary vortices can also form tertiary vortices by the same process. Outboard of the secondary vortex the flow reattaches and approaches the leading edge. At the leading edge the flow again separates and joins the flow from the lower surface in the shear layer.

Wind tunnel studies [20–22] have found that the leading-edge shear layer can become unstable and form small-scale vortices about the primary vortex as sketched on the right hand side of Fig. 6. The small-scale vortices begin at the outer edge of the sheet and follow a spiraling path until, at some distance downstream, they coalesce along the outer edge of the vortex core. The three-dimensional structure is steady in time in the experiments. Laser-Doppler anemometry measurements in the crossflow plane on a delta wing [23, 24] define quantitatively the series of vorticity concentrations about the primary vortex due to these longitudinal structures.

The presence of the primary vortex affects the local velocity and pressure distributions on the wing to a large extent by inducing additional velocities, the predominant

effect being a low-pressure region underneath the position of the vortex core. It is mainly this suction peak giving rise to “vortex lift” [25] in addition to that achieved with fully attached flow (“potential lift”). As a result the relation between lift and incidence is nonlinear. The extent of the effect of secondary separation on the surface pressure distribution depends strongly on whether the boundary layer is laminar or turbulent. Secondary separation effects are largest for the laminar case [26]. In general, the presence of the secondary vortex may influence the location of the primary suction peak such that it is not located exactly below the location of the primary vortex core. The spanwise variation of pressure over the lower (windward) surface is essentially constant and higher than the freestream pressure.

The leading-edge vortices as well provide the central parts of the wing with “fresh air”, counteracting the tendency to two-dimensional boundary layer separation, which is the prime factor for “stall” of conventional wings. Together with the suction effect of the strong and stable leading-edge vortices this is the reason for the lift coefficient curve for a delta wing exhibiting an increase in  $C_L$  for values of  $\alpha$  at which conventional wing planforms would be stalled. The typical maximum lift coefficient  $C_{L\max}$  of a highly swept delta wing is on the order of 1.0 to 1.4, depending mainly on the sweep angle. Between 30% and 60% of the total lift at high alpha is produced by the leading-edge vortices [27].

Ultimately, as angle of attack is further increased, a limit to the above-described favorable effects induced by the vortex system is reached when large-scale vortex breakdown occurs above the wing, which renders the flow field unsteady.

### 3.2. Vortex Breakdown

The vortex breakdown mechanism is rather involved and is one of the unresolved problems in fluid mechanics [1]. Therefore, only some descriptive experimental results describing the physical characteristics of vortex breakdown will be included here. For excellent surveys on the topic, see Délery [28], Nelson and Pelletier [29] and Gur-sul [30, 31].

The rather spectacular phenomenon of vortex burst or breakdown was first visualized by Werlé [32] in a water tunnel and was later confirmed by Peckham and Atkinson [33] and Elle [34]. Elle discovered that the core of a leading-edge vortex suddenly expands in cross-sectional area when the incidence is increased beyond a critical angle, which he found to depend on the sweep angle of the wing. At lower angles, the vortex may be bursting but the burst point is downstream of the trailing edge and does not affect the vortex lift on the wing. In general, bursting involves a sudden decrease in the magnitude of the axial and circumferential velocity components of the core, as was first observed by Lambourne and Bryer [35]. More detailed measurements by Kegelman and Roos [36, 37] and Délery [28] showed that on the vortex axis the axial component of the velocity is increasing up to the breakdown location where it decreases abruptly. Axial velocities of more than three times the freestream velocity were measured in the vortex core upstream of breakdown by Payne *et al* [38].

In experiments [24, 39] it has been observed that breakdown can be postponed for a given adverse pressure gradient by axial air blowing, i.e. by increasing the maximum value of the jet-like axial velocity profile. In the vortex core the total-pressure loss is

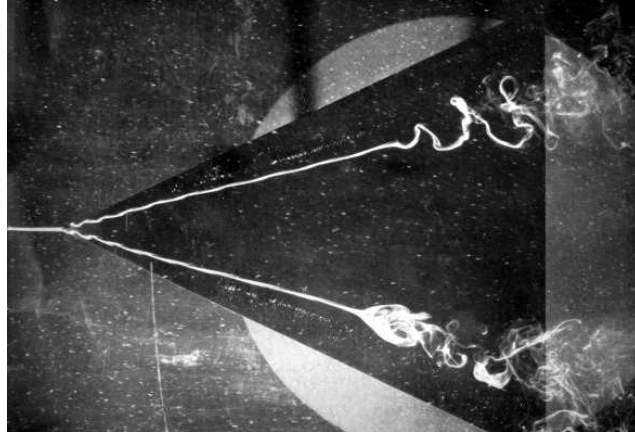


Figure 7: Water-tunnel visualization of spiral (top) and bubble-type (bottom) vortex breakdown over a delta wing [35]. The two streaks of dye are at the center of strong vortices shed from the wing's leading edges

also about constant up to the breakdown location where it increases sharply. The portion of the core with high losses in total pressure decreases up to the burst location, increases abruptly at the location of the burst and then starts to fill the entire vortex core. In this area the total pressure losses start to decrease again. During breakdown, the mean rotational vorticity vector changes from an essentially longitudinal direction to a generally tangential direction. In other words, the vorticity, which is at first oriented in the x-wise direction and concentrated near the vortex axis, tends to migrate in regions out of the axis and to reorient itself along a transverse direction.

Several types of breakdown have been identified. Lambourne and Bryer [35] were the first to distinguish spiral and bubble type breakdown. A water-tunnel visualization of both types of breakdown is presented in Fig. 7. In the spiral type of breakdown a rapid deceleration of the core flow takes place. Immediately downstream, the vortex core filament abruptly kinks and starts to spiral around the axis of the structure, forming a corkscrew-like distortion of the vortex core. The spiral structure can persists for one or two turns before breaking up into large-scale turbulence [40]. For leading-edge vortices the sense of the spiral winding is opposite to the direction of rotation of the upstream vortex, however, the rotation of the winding is in the same direction as the rotation of the upstream vortex. This is illustrated in Fig. 8. The bubble type is characterized by a stagnation point on the vortex axis followed by an oval-shaped recirculation zone. The upstream half of the recirculation zone can be nearly axisymmetric with the core flow spreading out symmetrically at the stagnation point and passing smoothly around the recirculation zone. The downstream half, however, is usually open and irregular with the flow shedding from the aft end as if from a blunt solid body [40]. Payne *et al* [38] observed that the bubble is single-celled with the recirculation flow moving upstream along the vortex axis. The bubble is usually two or three (upstream) core diameters in length. Downstream of the bubble the

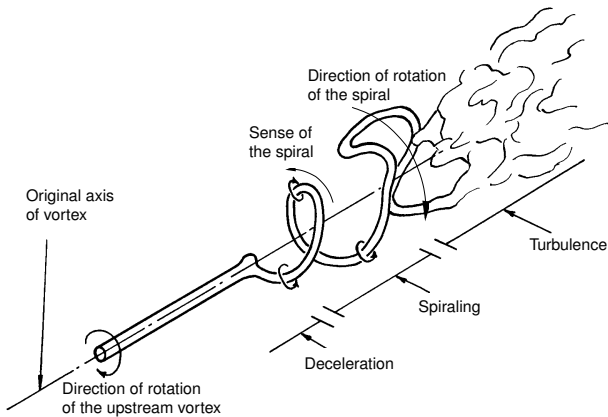


Figure 8: Spiral breakdown: stages in behavior of axial filament and sense of the spiral [35]

vortex is turbulent and diffuses rapidly with distance. The flow parameters that affect these two types of vortex breakdown, and the physical process of the breakdown mechanism, are still among the most challenging fundamental research problems in fluid dynamics [1]. Some investigators think that the bubble form is basic, the spiral type being a consequence of the instability of the bubble form. Others think that the bubble type is an artifact of the visualization technique used, e.g. Greenwell [41].

After breakdown is first located over the wing near the trailing edge, further increase in incidence provokes rapid displacement of breakdown in the forward direction at first; then more slowly with increasing angle of attack. Huang and Hanff [42] could demonstrate that delta wings with sweep angles between  $55^\circ$  and  $75^\circ$  exhibit a more gradual movement of the vortex burst location over the trailing edge than reported by Wentz and Kohlman [43], agreeing with findings by Lowson and Riley [44] and Délery [28]. Furthermore, the breakdown point over the trailing edge of a  $70^\circ$  delta wing proved to remain quite stable confirming that the so-called “knee phenomena”, characterized by a rapid, almost abrupt jump of the breakdown location from the trailing edge to mid-chord (Wentz and Kohlman [43]) are atypical (Lowson and Riley [44]) and cannot be confused with possible discontinuities associated with the presence of a leeside edge bevel.

Increased leading-edge sweep decreases the leading-edge vortex strength (Hemisch and Luckring [45]) and delays vortex breakdown. Wentz and Kohlman [27] found that for sweep angles higher than  $75^\circ$ , breakdown becomes independent of the sweep angle. Furthermore, the coupling between vortex burst and lift is not strong for wings with sweep angles of  $70^\circ$  or less (Kegelman and Roos [36]), i.e. the first occurrence of vortex breakdown over a delta wing does not correspond to maximum lift, as commonly assumed in numerous textbooks. The primary effect of burst rather appears to be a slight reduction of the local growth rate of the vortex.

The leading-edge shape significantly affects the location of leading-edge vortex burst, even for thin, flat plate delta wings (Kegelman and Roos [36], and Miao *et al* [46]). The differences can be attributed to the variation in the local leading edge separation and the strength of the resulting vortex. The effect of the leading-edge shape on the flow pattern decreases with increasing Mach number. Wentz and Kohlman [27] found no significant differences in breakdown characteristics for delta wings of given sweep with plain, diamond, arrow and cropped planform. Positive camber was found to delay breakdown. Breakdown was seen to occur earlier with thicker wings for given flow conditions.

The flow upstream of breakdown is steady, whereas numerous researchers have observed unsteady flow downstream of the burst point, e.g. Délery [28], O’Neil *et al* [47]. The experimental and computational breakdown location itself has also been observed to dynamically oscillate about 5% root chord for a 70° delta wing, as was reported by Agrawal *et al* [48] and Mitchell [24], e.g.. Payne *et al* [38, 40], on the other hand, who performed wind-tunnel test on thin, sharp leading edge, flat-plate delta wings having sweep angles of 70°, 75°, 80°, and 85°, reported that the breakdown point was relatively steady and symmetric on both sides of the 70° wing at  $\alpha = 40^\circ$  except for a high frequency low magnitude oscillation. However, with increasing leading edge sweep they found the breakdown locations to become increasingly asymmetric and unsteady. Breakdown was observed to wander back and forth over about half of the chord length on the 85° model when the freestream velocity was as low as 3.05 m/s. When the freestream velocity was increased above 7.62 m/s the position of the breakdown would stabilize, although the asymmetry in location between the left and right sides would remain. This finding was confirmed by Mitchell [24, 39], who observed that as the freestream velocity is augmented, the amplitude of the oscillations is diminished, resulting in a more stable vortex breakdown location. Increasing angle of attack was found to have the same effect. Further, Mitchell’s data also indicated an interaction between the two leading-edge vortices, which caused the breakdown locations on each side of the wing to oscillate out of phase. As the breakdown location on one side of the wing moved aft, the other tended to move forward and vice-versa. This breakdown location asymmetry is illustrated in Fig. 9.

Breakdown has to be provoked by a destabilizing agent, like the longitudinal adverse pressure gradient in the region of the trailing edge, which in turn is a function of incidence and sweep, e.g. Erickson [49] and Lambourne and Bryer [35]. Elle [34] related breakdown to the shedding of vorticity from the leading edges developing in such a way that the downstream transport of fluid in the vortex core fails: when the vorticity-feeding rate from the leading edge exceeds what can be convected downstream, the vortex filaments tighten up leading to breakdown (Huang and Hanff [42]). Lawson [50] was the first to suggest that the final position of an established vortex breakdown be governed by different parameters from those which cause the initial formation. He suggested that the final breakdown point depends on the adverse pressure gradient connected with the trailing edge. The unsteady mixing in the breakdown zone dissipates vorticity and causes a turbulent wake as well as loss of lift.

Vortex breakdown does appear to depend rather weakly on Reynolds number (Lambourne and Bryer [35]). The latter may suggest that in essence it is an inviscid flow phenomenon. But several researchers measured a more forward breakdown point

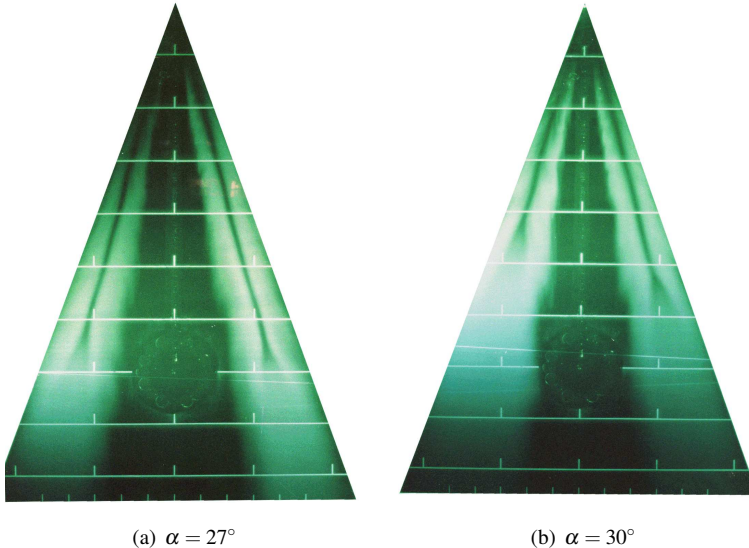


Figure 9: Laser sheet visualization of symmetric (a) and asymmetric (b) vortex breakdown ( $U_\infty = 24$  m/s,  $\beta = 0$ ). Reproduced from [24], with permission.

with an increasing Reynolds number. Soltani and Bragg [51] found that for sharp-edged wings the Reynolds number effects appear to be restricted to angles of attack where the burst point moves onto the wing. They report as well that maximum lift increases with decreasing Reynolds numbers. At a Reynolds number based on running length of  $0.8 \times 10^6$  to  $0.9 \times 10^6$ , boundary layer transition occurs and the secondary separation line moves out towards the leading edge (Kjelgaard *et al* [52]). Thicker wings may be more Reynolds-number sensitive, according to Wolffelt [53]. Significant Reynolds number effects were as well observed by Erickson [49] for wings with “round leading edges, deflected flaps, thick sections, where leading edge flow separation is delayed and a salient edge of separation does not exist.”

Despite the dramatic changes in the flow field over a delta wing associated with breakdown the global strong circulatory flow pattern does not disappear abruptly at the point where vortex breakdown occurs, it still persists (Hummel [54]). Upstream of this point the vortex is hardly affected. Délery [28] suggested that the secondary vortex is not affected by the breakdown of the primary vortex. However, breakdown is indicated by a kink in the secondary separation line (Huang and Hanff [42]). A variety of reverse flow patterns have been observed by Huang and Hanff [42] when breakdown was near or at the apex. Earnshaw and Lawford [55] observed a “whorl” near the outboard tip for the same flow conditions. The suggested vortex system and the corresponding surface pattern are sketched in Fig. 10.

When the angle of attack is larger than the one that corresponds to the breakdown location at the apex, the shear layer separating from the leading edges will not be able to form swirling flow with axial motion. Instead, vortex shedding from the wing will start [56].

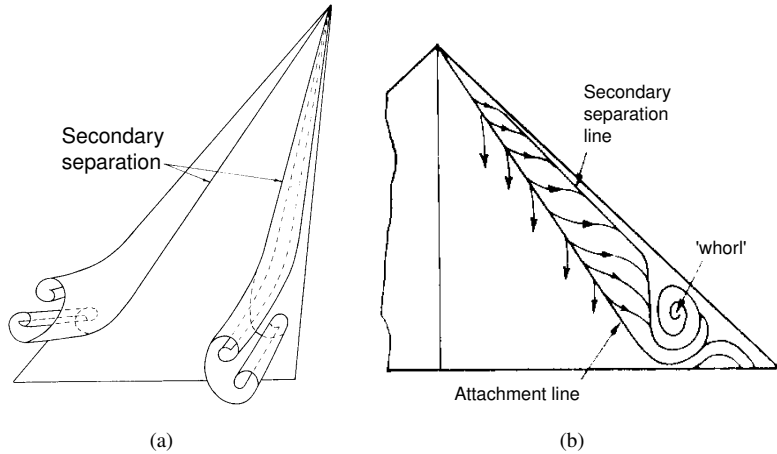


Figure 10: Suggested secondary vortex system (a) associated with 'whorl' upper surface skin friction pattern (b) at high incidence angles [55]

### 3.3. Previous Numerical Studies

In the following, CFD studies of vortex flow over delta wings are reviewed. This review is by no means complete and focuses mainly on simulations at high angle of attack, where vortex breakdown occurs.

#### 3.3.1. Steady-State Simulations

Eriksson and Rizzi [57] pioneered the solution of the compressible three-dimensional Euler equations for the subsonic and transonic flow around a semi-span  $70^\circ$  delta wing with sharp leading edges. They employed an O-O type grid with two singular lines, constructed by transfinite interpolation, to discretize the model and flow field with about 18,000 grid points. A finite-volume approach that uses an explicit local time-stepping scheme together with centered space differences was then used to obtain steady-state solutions to the Euler equations in integral conservation-law form at freestream Mach numbers of  $M_\infty = 0.9$  and  $M_\infty = 1.5$ . Their solutions at  $\alpha = 15^\circ$  angle of attack clearly show leading-edge separation and the presence of a vortex. The vortex sheet, smeared out over a number of grid cells, was obtained automatically as part of the numerical solution. Numerical dissipation was later [58] made responsible for enforcing the separation at the sharp leading edge. In deference to physical viscosity, the amount of numerical viscosity in an Euler code is determined by the numerical algorithm, by the grid topology and grid size, and by the variation of flow variables [1]. In addition to these are the effects of the artificial dissipation terms introduced into the calculation to avoid spurious oscillations and to capture shocks.

In the Euler solution of Rizzi and Eriksson [59] and Rizzi *et al* [60] a vortex was also found at the rounded leading edge of a delta/arrow wing. The authors stated

in [61] that artificial viscosity was responsible for the formation of the vortex due to the shedding of a vortex sheet from the smooth surface.

Rizzi and Eriksson [62] solved the incompressible Euler equations for the flow around a  $70^\circ$  delta wing at  $\alpha = 20^\circ$  using an artificial compressibility method. They used their O-O type grid with two singularities and a total of 76,800 cells. Their comparison with the results of a potential boundary-integral (panel) method was the first quantitative demonstration that a vortex sheet separating from a swept leading edge can be captured in the vorticity field of a solution to the Euler equations with a reasonable degree of realism. In this study the occurrence of an abrupt change in the circumferential velocity component at about 80% chord position was interpreted as an “additional, and unexpected, vortex phenomenon”. The vorticity and axial velocity contour plots suggest, however, that vortex breakdown was probably predicted for the first time in a numerical solution to the Euler equations.

In a subsequent grid refinement study reported in [2], Rizzi and Engquist produced an incompressible Euler solution with the artificial-compressibility method on a grid with 640,000 cells. As in the previous study [62], the vorticity contours reveal that the straight vortex core develops into a helical spiral ahead of the trailing edge “and splits into a number of subsidiary vortices.” Rizzi and Engquist explained this phenomenon with a vortical instability resembling instability vortices in separated free shear layers. They rule out “full-blown vortex breakdown” because the vortex core does not expand substantially.

The first confirmed description of vortex breakdown in an inviscid numerical solution to the Euler equations was given by Sirbaugh [63]. He observed a sudden expansion of the particle traces over a  $65^\circ$  cropped delta wing at an incidence angle of  $21^\circ$  and  $M_\infty = 0.85$ . Cross plane views of the velocity field and vorticity contours showed the expansion of the vortex and the spreading of vorticity over the aft part of the wing. A similar significant change in the flow field, calculated from solutions of the Euler equations for flows over a delta wing, was also observed by Scherr and Das [64] and interpreted as indicating the appearance of vortex breakdown.

Rizzi [65] was first to use an O-O type grid with more than one million grid points to compute three-dimensional solutions to the Euler equations. In his study of a  $70^\circ$  delta wing at  $\alpha = 15^\circ$  and  $M_\infty = 0.7$  and  $M_\infty = 1.5$ , he demonstrated that a grid much denser than 50,000 grid points is required to capture the rich structure of the vortex flow interacting with a shock. More relevant to the present study, Rizzi also showed that in comparison with standard-size grids, the suction peak under the vortex is markedly stronger on the fine grid.

In [61], Rizzi and Purcell concluded that for the case of a flat  $70^\circ$  delta wing of zero thickness,  $\alpha = 10^\circ$  and  $M_\infty = 0.7$ , they nearly reached grid convergence on an O-O type grid with just over one million grid cells using the compressible Euler code of Rizzi and Eriksson [59]. They also found non-stationary behavior in the Euler solution of the transonic flow around a cranked and cropped delta wing with round leading edges at  $8^\circ$  angle of attack. They related this unsteadiness to “vortex instability or bursting” at the crank of the twisted wing.

Looking at the total pressure deficits developing in their Euler solutions of the flow over delta wings, Murman and Rizzi [58] suggested that a rational prediction of the boundaries of vortex bursting may be possible from computational solutions of the

Euler equations. Their reasoning was that the total pressure deficits are large enough that the streamline on the vortex axis may not be able to overcome an adverse static pressure gradient without stagnating.

An early calculation of the flow about a slender delta wing by the solution of the Navier-Stokes equations using the thin-layer approximation was presented by Fujii and Kutler. The thin-layer Navier-Stokes equations were solved by an implicit non-iterative approximate factorization scheme of Beam and Warming. The computation was done for a  $76^\circ$  delta wing, with a maximum chord thickness of 1%, the symmetry condition was then imposed and the grid used  $38 \times 51 \times 31$  grid points. The calculations were done for  $\alpha = 20.5^\circ$  and a Reynolds number of  $Re = 0.9 \times 10^6$ , assuming laminar flow in the Navier-Stokes formulation. This calculation captured the primary leading-edge vortex as well as the secondary vortex and agreed reasonably well qualitatively with experimental results.

A comparison between Euler and laminar Navier-Stokes solutions for the transonic flow over the round-edged  $65^\circ$  delta wing of the International Vortex Flow Experiment at  $10^\circ$  angle of attack was done by Rizzi *et al* [66, 67]. Both solutions showed the development of a vortex shed from the round leading edge. In the laminar solution the vortex started at the apex of the wing, whereas it started about one quarter chord downstream in the Euler solution, suggesting the action of different mechanisms for primary separation. Different mechanism were also seen at work in the secondary separation, due to the action of the boundary layer in the laminar case, and due to the losses brought about by a cross-flow shock in the inviscid case. In the laminar solution the position of the primary vortex core and the pressure level under it were predicted in good agreement with experimental measurements, whereas the suction peak in the Euler solution was found to be too high and to lie too close to the leading edge. This was also found in e.g. a study by Raj *et al* [68] of the  $M_\infty = 0.3$  flow around a  $63^\circ$  sharp edge cropped delta wing at  $\alpha = 19.95^\circ$  using an explicit finite volume Euler code.

An improved solution of the incompressible Navier-Stokes equations for a flow over a delta wing was presented by Hartwich *et al* [69]. The thin-layer approximation was solved by an upwind scheme based on flux-difference splitting using the Baldwin-Lomax turbulent model with the Degani-Schiff modification in the massive separation regions. Central differencing of the viscous shear fluxes and a total variation diminishing (TVD)-like discretization of the inviscid fluxes yield second order spatial accuracy. The flow over a delta wing of aspect ratio one at  $M_\infty = 0.3$ ,  $\alpha = 20.5^\circ$  and  $Re = 0.9 \times 10^6$  was calculated and the results compared with experimental data. The flow field was discretized using an H-C grid. The calculated surface streamlines revealed the primary separation along the sharp leading-edge and its reattachment near the centerline, the induced secondary separation line followed by the reattachment line very close to the leading-edge. The calculated pattern was compared with the surface oil flow pattern obtained experimentally and showed good agreement. Also the spanwise pressure distributions at various chordwise stations, including the pressure variation due to the secondary separation, agreed reasonably well with experimental data thanks to a simple transition model. The calculation of the lift and pitching moment coefficient variation with an angle of attack up to  $40^\circ$  showed excellent agreement with experimental data over the complete angles of attack range, including the

diminishing of lift due to vortex breakdown onset at the trailing edge at  $\alpha = 30^\circ$ . Particles traces along the vortex core, integrated for the solution at  $\alpha = 40^\circ$ , were seen to suddenly expand at about 40% of the chord, destroying the core and resulting in breakdown into a bubble-shaped region of reverse flow.

The vortex breakdown of a  $75^\circ$  swept delta wing at  $M_\infty = 0.3$  and  $Re = 10^6$  was studied by Ekaterinaris and Schiff [70, 71]. The flow at  $\alpha = 32^\circ$  was computed with a  $57 \times 54 \times 70$  point cylindrical grid using the zonal method. The calculations predicted bubble type breakdown, which was visualized by streamlines starting from the wing apex. At a higher angle of attack of  $40^\circ$ , a calculation was made using a spherical, single block grid of  $112 \times 105 \times 70$  points. The flow was seen to be very similar to that obtained for  $\alpha = 32^\circ$ , except that the burst point was located further upstream towards the apex. In further numerical experiments reported by Ekaterinaris and Schiff vortex breakdown was not observed when a coarse grid of  $33 \times 30 \times 35$  points was used for calculations of the flow field over the  $75^\circ$  delta wing at angle of attack above  $35^\circ$ . With somewhat better grid resolution, but still using a relatively coarse grid of  $33 \times 54 \times 35$  points, breakdown was observed. However, in the calculations with the coarse grid resolution, the position of the burst point was predicted to be further downstream and the extent of the vortex breakdown was much smaller than calculated with the fine grid resolution. This study of Ekaterinaris and Schiff also calculated the strong effect of the adverse axial pressure gradient on vortex breakdown. It was shown that eliminating the effect of the adverse axial pressure gradient by excluding the wake region from the computations, vortex breakdown was eliminated from these calculations. An additional investigation involved the possible existence of unsteadiness in the region downstream of the tip of the bubble type breakdown. No such unsteadiness was observed for the bubble type vortex breakdown on the delta wing. However, there was evidence of self-excited unsteady flow behavior in the case of the spiral type breakdown observed by Fujii and Schiff [72] over a  $80^\circ/60^\circ$  double delta wing at  $M_\infty = 0.3$ ,  $\alpha = 35^\circ$  and  $Re = 1.3 \times 10^6$ .

A summary of results of the former Western European Armaments Group (WEAG) TA15 program was presented by Arthur *et al* [73]. The investigation, which was concerned with the investigation of both the inviscid and viscous flow over a cropped delta wing and the benefits of using grid adaption, confirmed the inadequacy of the Baldwin-Lomax turbulence model (with Degani-Schiff modification) for the computations of flows of this type. An earlier Common Exercise [74] was concerned primarily with the investigation of viscous flow over the configuration without recourse to grid adaption. It highlighted the need to use a grid of appropriate grid topology.

Using the unstructured Euler and Navier-Stokes code USM3D, Pirzadeh [75] showed that the numerical prediction of vortex flow and vortex breakdown over a  $65^\circ$  delta wing was highly sensitive to the local grid resolution. He also stated that solution adaptive grid refinement is essential to the application of CFD to these complicated flow fields.

### 3.3.2. Time-accurate Simulations

Gordnier [76] performed time-accurate laminar computations of the  $M_\infty = 0.2$  flow over a stationary full-span<sup>2</sup>  $65^\circ$  delta wing at  $\alpha = 27^\circ$  and roll angles of  $0^\circ$  and  $-4^\circ$ . He investigated the effects of solution scheme, time-step size and grid resolution on the computed results. Using a first-order accurate time-stepping scheme, he found that a non-dimensional time step of 0.0005 and grid spacings on the order of  $0.005c - 0.01c$  in the axial direction over the wing were required to adequately resolve the primary features of vortex breakdown for a Reynolds number of  $Re = 3.2 \times 10^4$ . Analysis of the structure of vortex breakdown for the  $-4^\circ$  roll case showed predominantly spiral-type breakdown occurring, with the breakdown locations varying in the axial direction with time. Bubble-type breakdown was observed for short periods during transient upstream movements of the breakdown location.

Visbal [77] investigated the onset and unsteady structure of spiral vortex breakdown over a semi-span  $75^\circ$  delta wing at  $M_\infty = 0.2$  and  $Re_c = 9,200$  by solving the full unsteady Navier-Stokes equations utilizing an implicit, time-accurate Beam-Warming scheme. The accuracy of the numerical solutions was established through examination of the effects of grid resolution and time-step size on the computed flow field and by favorable agreement with experimental data. For the static cases in the angle of attack range  $17^\circ \leq \alpha \leq 34^\circ$ , Visbal found vortex breakdown to first emerge in the near wake as a nearly-axisymmetric bubble. The bubble was seen to propagate upstream onto the wing with increasing angle of attack. It subsequently transformed into a rotating spiral structure. Visbal elucidated kinematic aspects of the flow in terms of pathlines and streaklines, as well as by critical-point analysis of the mean and instantaneous velocity vector field. He concluded that, contrary to common assertions, spiral breakdown does not exhibit a three-dimensional stagnation point in front of the region of axial flow reversal. Coherent pressure fluctuations and unsteady secondary boundary layer separation were related to a strong interaction between breakdown and the boundary layer on the wing.

In another unsteady simulations of spiral vortex breakdown over a  $75^\circ$  delta wing at  $\alpha = 32^\circ$ ,  $M_\infty = 0.2$  and  $Re_c = 9,200$ , Visbal [78] demonstrated that on a given grid of H-H topology higher-order schemes predict a much richer structure corresponding to a stronger, tightly wound spiral.

Simulations of unsteady cases in the scope of the previously mentioned WEAG TA15 Program have been restricted to the wing only, with the fuselage neglected. Although these results were encouraging, they were limited to low  $\alpha$  [6]. The turbulence model used (Baldwin-Lomax with Degani-Schiff modification) was the same as that found to be inadequate for steady flow.

Müller and Hummel [79] performed a time-accurate Euler calculation of a half-span model of the VFE-configuration at  $M_\infty = 0.2$  and  $\alpha = 20^\circ$ . The calculations predicted periodic oscillations of the force and moment coefficients caused by rotating spiral-type vortex breakdown. They found a considerable influence of the 4<sup>th</sup>-order artificial damping coefficient on all unsteady characteristics and the breakdown position in particular. In a follow-up study, Müller and Hummel [80] analyzed the unsteady,

---

<sup>2</sup>To the knowledge of the author, this is the first time-accurate CFD study of vortex breakdown over a full-span stationary delta wing.

burst vortical flow over the same cropped delta-wing geometry at large angles of attack  $\alpha > 18^\circ$  by time-accurate Euler and Navier-Stokes calculations. The 4<sup>th</sup>-order artificial damping coefficient was “calibrated” for the Euler and Navier-Stokes calculations using the Baldwin-Lomax turbulence model such that they predicted the experimentally measured breakdown position. Müller and Hummel found that compared to Navier-Stokes results, the discretized Euler equations predict a further downstream vortex breakdown location and higher dominating frequencies. They used different grids, however, for the Euler and Navier-Stokes calculations, which might explain these differences. For higher angles of attack the differences were shown to diminish. Unfortunately, they did not perform any grid studies.

Morton *et al* [81] reported Detached-Eddy Simulations (DES) of a sharp-edge 70° delta wing experiencing vortex breakdown at  $M_\infty = 0.07$ ,  $Re = 1.56 \times 10^6$  and  $\alpha = 27^\circ$ . The commercial CFD code COBALT was used to conduct a time-accuracy and turbulence model study on an unstructured grid with 2.45 million cells. The DES solutions were shown to be sensitive to time accuracy in the frequency domain but achieved an asymptotic solution as the time step was reduced. The Spalart-Allmaras and Menter Shear Stress Transport models were shown to add too much turbulent eddy viscosity to the core of the vortex, making them inadequate for capturing the physics of vortex breakdown at high Reynolds numbers correctly. DES and Spalart-Allmaras with rotational correction terms, on the other hand, captured the full spectrum of frequencies and compared very well with experimental vortex breakdown location and turbulent kinetic energy data. In a follow-up DES study for the same wing and flow conditions, Morton *et al* [82] demonstrated that a tangibly wider range of turbulent length scales is captured on successively finer grids. Coarse, medium and fine grids were run using COBALT. The solution on the medium and fine grid showed evidence of additional vortex structures winding around the primary vortex up to the breakdown position. These structures are probably instability vortices like the ones illustrated in Fig. 6. The breakdown location was seen to vary with grid density, moving slightly aft as the grid was refined. In yet another DES study, Mitchell *et al* [83] confirmed the formation and existence of spatially stationary, co-rotating vortical substructures in the separated shear layer feeding the primary vortex. Five unstructured grids were used, the coarsest one having 1.2 million cells and the finest one having as much as 10.7 million cells. Apart from resolving the substructures, the finer grids also captured an increased number of structures in the post-breakdown region, as well as spanwise vortical structures being shed from the blunt trailing edge. Very coherent vortical substructures around the vortex core were predicted both upstream and downstream of the vortex breakdown location using automatic mesh refinement.

Recently, Estorf and Hummel [84] performed Euler and Navier-Stokes calculations of the unsteady flow over the full-span VFE-1 65° delta wing at  $M_\infty = 0.2$ ,  $Re = 1.55 \times 10^6$  and  $\alpha = 25^\circ$  using the structured FLOWER code. Turbulence was modeled with the Baldwin-Lomax model with Degani-Schiff modification. Spiral-type breakdown was calculated for both sides of the wing. Even for symmetric boundary conditions both the Euler and Navier-Stokes solutions exhibited an asymmetry in the left and right vortex breakdown location, as well as phase differences in the rotation of the spiral vortex axes. The asymmetry was also reflected in amplitude and phase differences between the left and right semi-span lift coefficients.

## 4. Computational Approach

The two CFD codes that have been used throughout the course of this thesis, NSMB and Edge, are presented below. These research codes feature several novel CFD methods, such as higher-order schemes, advanced turbulence models, detached-eddy simulation and adaptive grid refinement. The presentation of the codes is followed by a discourse on the Recursive Projection Method, a novel CFD method that has been developed to make unsteady computations with Edge more affordable.

### 4.1. The Structured Navier-Stokes Multi Block Code NSMB

The structured Navier-Stokes Multi Block solver (NSMB) [85–90] was initially developed at the Swiss Ecole Polytechnique Fédérale de Lausanne (EPFL) in 1991. Since June 1992, it is being developed in a joint research project between two universities (EPFL-IMHEF and KTH), one research establishment (CERFACS, Toulouse, France) and two industrial partners (EADS/Airbus, Toulouse, France and Saab Aerospace, Linköping, Sweden). In 2000, two further partners joined the development team, the Ecole Nationale Supérieur d’Arts et Métiers (ENSAM-SINUMEF), Paris, France, and CFS Engineering, Lausanne, Switzerland. The objective of this industry-driven project is to make the very computationally-intensive Navier-Stokes simulation of full aircraft practical for industry to use at acceptable costs in design work.

NSMB solves the compressible Navier-Stokes equations using a finite volume method on structured meshes. The multi-block approach facilitates the treatment of complex geometries, and allows a straightforward parallelization of the code with the blocks distributed on different processors of a parallel computer.

The Navier-Stokes equations are discretized in space on structured grids using either a first, second, or third order upwind scheme (Total Variation Diminishing (TVD) version of Roe’s scheme [91], AUSM and AUSM+ scheme), or a second or fourth order space centered scheme according to Jameson *et al* [92] using artificial dissipation (standard Jameson dissipation, Martinelli dissipation or Matrix dissipation).

The equations are integrated in time using explicit Runge-Kutta time stepping, or the implicit LU-SGS scheme [93, 94] using scalar or matrix approximation. Convergence acceleration procedures such as local time stepping, implicit residual smoothing and multigrid can be used for steady-state calculations, while dual time stepping is available for time accurate calculations. For incompressible flows the preconditioning technique by Turkel [95] has been implemented to remove the stiffness in the system of equations. This technique can be combined with the standard convergence acceleration and time integration schemes.

Either the implicit LU-SGS scheme or the explicit Runge-Kutta scheme can both be used for unsteady calculations. In addition, the dual time stepping approach by Jameson employs either one of these two schemes as a steady-state driver in the inner loop.

Various turbulence models of different complexity are available in NSMB, and have been thoroughly tested. They include algebraic models such as the models of Baldwin-Lomax and Granville, the one-equation model by Spalart and Allmaras, the two-equation  $k - \varepsilon$  model by Chien and Hoffman, the  $k - \tau$  model by Speziale, and

different  $k - \omega$  models. Large-Eddy Simulation (LES) and Detached-Eddy Simulation (DES) are also available. The turbulence models are described in detail in the NSMB handbook [85] and in [88, 96].

The so-called Arbitrary Lagrangian Eulerian (ALE) method is implemented into NSMB [90, 97]. It can be used to simulate wings in motion. Recently, the ALE implementation was extended to sliding meshes. NSMB is also capable of patched grid [98] and Automatic Mesh Refinement (AMR), both of which can be used to enrich the numerical grid in areas of interest (AMR however requires coupling to the surface representation, i.e. the database, and communication routines exist only so far for DAMAS, not for MEM-COM, that latter being used at KTH (see MEM-COM description below)). Multigrid [99] and full multigrid can be used for convergence acceleration.

The code is written in Fortran 77. It has been developed on top of the MEM-COM data base system [100]. MEM-COM is an object-oriented data management system for memory and memory-to-disk data handling. The principal advantage of using MEM-COM is that for large-scale multi-block flow simulations, access to the independent blocks is extremely fast, and almost independent of the block number. The MEM-COM library includes a Dynamic Memory Manager (DMM), which offers the possibility to allocate the necessary storage of the arrays at run time. In the latest version of NSMB, Fortran 90 modules are used to allocate variable storage at run time. It is now also possible to write solution files at different times in `plot3d` or `quickview` format.

The NSMB solver has been parallelized in the ESPRIT III Project “Parallel Aero”, and a good speed-up has been obtained on different parallel platforms. Parallelization is achieved using the message passing communication model MPI. The code is optimized for both vector and RISC architectures using a preprocessor that transforms the most time consuming loops in either long vector loops over all grid points or into three loops over the  $i$ -,  $j$ -, and  $k$ -directions.

## 4.2. The Unstructured Flow Solver Edge

Edge [101–104] is a flow solver for unstructured grids of arbitrary elements under development by the Swedish Defence Research Agency (FOI/FFA) and others, among them KTH.

The solver is based on an edge-based formulation for arbitrary elements and uses a node-centered finite-volume technique to solve the three-dimensional compressible Reynolds-averaged Navier-Stokes equations. The control volumes are non-overlapping and are formed by a dual grid obtained from the control surfaces for each edge. This is illustrated in Fig. 11 All elements are connected through matching faces.

The governing equations are integrated explicitly towards steady state with a multi-stage Runge-Kutta scheme. The convergence can be accelerated with agglomeration multi grid, implicit residual smoothing and the Recursive Projection Method, which is described in detail in chapter 4.3. Low Mach number preconditioning is also available. Spatial discretization of the convective fluxes is done either with central differences with artificial dissipation or with a second-order accurate upwind scheme of Roe flux difference splitting type. Three different limiters can be used with the latter scheme, the minmod limited, the van Leer limiter and the superbee limiter. For the

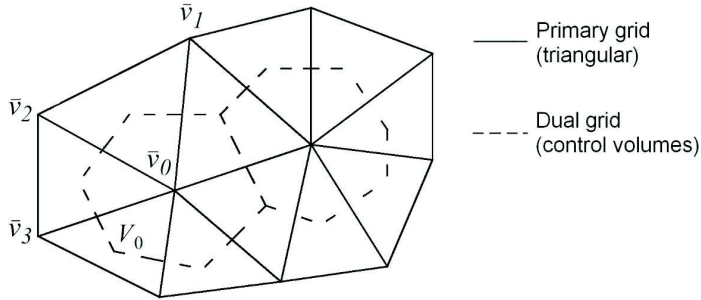


Figure 11: Schematic of a primary grid and its dual grid, consisting of polyhedral cells

viscous fluxes, a compact discretization of the thin-layer approximation or the fully viscous terms can be used. The thin-layer approximation only contains the normal derivatives of the viscous terms.

Several one- and two-equation turbulence models are available, among them the one-equation model by Spalart and Allmaras [105], Wilcox' standard two-equation  $k - \omega$  model [106] and several variants of it, including a low Reynolds number version, an explicit algebraic Reynolds stress model (EARSM) [107] and a differential Reynolds stress model (DRSM). A version of the EARSM with curvature correction is also implemented.

Time accurate calculations can be performed using either explicit Runge-Kutta time stepping with a global time step or implicit dual time stepping with explicit sub-iterations (dual time stepping [108]). A new algorithm that has been implemented into Edge to accelerate the convergence of the sub-iteration loop is described in chapter 4.3.

Automatic Mesh Refinement (AMR) can be used to refine the unstructured grid in regions of flow gradients when the grid was generated with Tritet [109, 110], the grid generation system accompanying Edge.

Edge is written in Fortran 90. All Edge data files are in the FFA (“Flexible Format Architecture”) format [111], which defines a structure for hierarchical data sets of a recursive, linked list form. Data files in FFA format may be binary (IEEE big endian) or in plain ASCII format. The parallel version of Edge uses MPI for message passing.

#### 4.3. The Recursive Projection Method

The Recursive Projection Method (RPM) is an iterative procedure that provides many of the desirable attributes of a Newton-based solution method to codes that only have fixed-point (Picard) iteration solvers. These attributes include robust convergence to both stable and unstable solutions and access to linear stability information. For instance, RPM can drive a code that only has an explicit time integration routine (a common Picard iteration scheme) to converge to a linearly unstable steady solution and provide approximations for the leading eigenvalues and eigenvectors.

### 4.3.1. Background and Previous Investigations

RPM was initially developed by Shroff and Keller at Caltech for bifurcation analysis [112]. It exploits the existence of a gap between the strongly stable and the slow Eigenvalues of the native Picard iteration scheme, which delay its convergence. RPM captures the few slow Eigenvalues by monitoring an approximate Krylov subspace formed by successive residuals of the native scheme and then performs Newton's method in the space spanned by the corresponding Eigenvectors, while still performing Picard iterations on the complement to that space. The method's main advantage is that it can be implemented easily on top of existing CFD codes and is capable of accelerating those codes.

Prior to the work of Schropp and Keller, the idea of splitting the iteration procedure was pursued by Rizzi and Eriksson [113], who employed an explicit smoothing algorithm followed by a Newton linearization of the solution projected onto a low-dimensional subspace to compute steady transonic flow. Jarausch [114] and Jarausch and Mackens [115, 116] performed the splitting using oblique projections based on singular subspaces. Davidson [117] considered a preconditioned RPM-type method, which required the evaluation of the Jacobian of the system to be effective. Lust [118] and Lust *et al* [119] obtained a hierarchy of different RPM related methods, known as Newton-Picard-Gauss-Seidel (NPGS) methods, by allowing several function evaluations per iteration.

There have been a number of CFD applications where RPM was used as a tool for bifurcation analysis. Keller and von Sosen [120] considered the incompressible Navier-Stokes equations, Tiesinga [121] used NPGS to analyze the incompressible cavity problem and Love [122] analyzed Kolmogorov and Taylor-Couette vortical flows. Burrage *et al* [123, 124] were among the first to use RPM as an acceleration method by applying it to linear systems of equations. Dorobantu *et al* [125] accelerated the computations of steady, quasi one-dimensional inviscid nozzle flow using RPM. This work was extended to two-dimensional compressible viscous flow by Möller [126]. More recently, Campobasso and Giles [127, 128] used RPM to stabilize and accelerate a linear Navier-Stokes solver for turbomachinery aeroelasticity.

Here, the main interest was in evaluating RPM as a method for accelerating the convergence of the inner time-stepping loop of dual time stepping. RPM is only one of several possible solution to accelerate dual time stepping. Hsu and Jameson [129], for example, have proposed an alternative implicit-explicit hybrid scheme, which uses dual time stepping to correct the solution obtained from an ADI formulation of the equations.

### 4.3.2. Derivation of the RPM Algorithm

The system of ordinary partial differential equations resulting from the spatial discretization of the Navier-Stokes equations is usually integrated in time using a fixed point iteration scheme of the type

$$u^{n+1} = F(u^n) \quad (1)$$

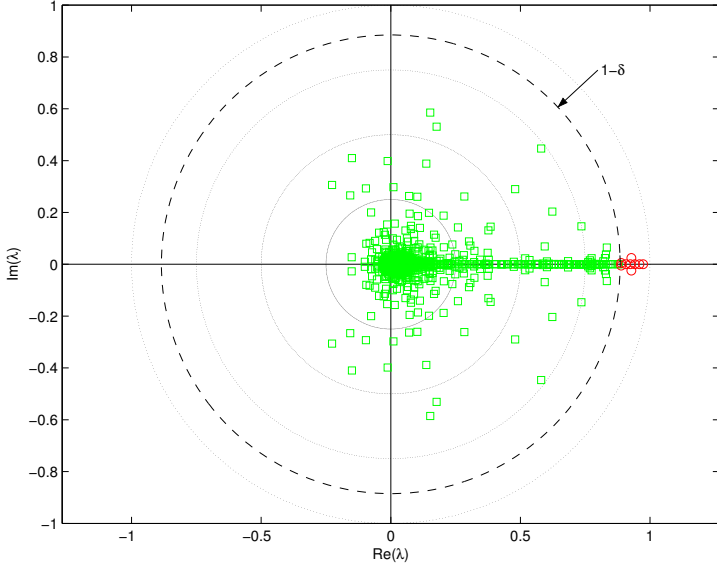


Figure 12: Spectrum  $\sigma$  of the Jacobian  $J(u^\infty) \equiv F_u(u^\infty)$  for a nozzle simulation; dominant Eigenvalues  $\lambda_1, \dots, \lambda_k$  captured by RPM in red (circles);  $\lambda_{k+1}, \dots, \lambda_N$  in green (squares); reproduced from [126], with permission

The rate of convergence of the scheme to a fixed point  $u^\infty$  will be slow if the modulus of the most dominant eigenvalue of the Jacobian  $J = F_u$  is close to one. The spectrum  $\sigma$  of the Jacobian evaluated at  $u^\infty$  is

$$\sigma[F_u(u^\infty)] \equiv [\lambda_i]_1^N \quad (2)$$

where  $N$  is the number unknowns. Following [112], we assume that this spectrum satisfies, for some small  $\delta > 0$ ,

$$|\lambda_1| \geq |\lambda_2| \geq \dots \geq |\lambda_k| > 1 - \delta \geq |\lambda_{k+1}| \geq \dots \geq |\lambda_N| \quad (3)$$

that is, we assume that there is a gap between the  $k$  dominant eigenvalues and the rest of the spectrum. This is true for the transport PDEs encountered in many engineering problems, where a separation of time scales translates into a gap in the spectrum of  $J(u^\infty)$ . Further suppose that the number of dominant eigenvalues  $k$  lying outside the disk  $K_{1-\delta}$  is small compared to  $N$ ,  $k \ll N$ . This is illustrated schematically in Fig. 12.

The RPM algorithm is based on the projection of Eq. (1) onto the orthogonal subspaces  $\mathbb{P} \subset \mathbb{R}^N$  and  $\mathbb{Q} \equiv \mathbb{P}^\perp$ , which are spanned by the eigenvectors of  $J(u^\infty)$  corresponding to the subset of the  $k$  dominant Eigenvalues and that of the  $(N - k)$  remaining ones, respectively. Denoting by  $V_p$  an orthonormal basis of  $\mathbb{P}$ , the orthogonal projectors  $P$  and  $Q$  of the subspaces  $\mathbb{P}$  and  $\mathbb{Q}$  are defined, respectively, as

$$P = V_p V_p^T, \quad Q = I - P, \quad (4)$$

where  $I$  is the identity matrix. When eigenvalues close to the unit circle are captured, the basis  $V_p$  is augmented with the current dominant Eigenmodes, and the projectors  $P$  and  $Q$  are updated accordingly. Thus, every  $u \in \mathbb{R}^N$  has a *unique* orthogonal decomposition

$$u = p + q, \quad p = Pu \in \mathbb{P}, \quad q = Qu \in \mathbb{Q} \quad (5)$$

and the fixed point problem, Eq. (1), can be decomposed into

$$u^{n+1} = p^{n+1} + q^{n+1} \quad (6a)$$

$$p^{n+1} = f(p^n, q^n) = PF(p^n + q^n) \quad (6b)$$

$$q^{n+1} = g(p^n, q^n) = QF(p^n + q^n) \quad (6c)$$

The  $Q$ -part of the split scheme has better convergence properties than the original scheme since the influence of the dominant Eigenvalues has been eliminated, however, the slow modes are still present in the  $P$ -part [126]. The idea behind RPM is to replace Eq. (6b) with an implicit relation,

$$p^{n+1} = PF(p^{n+1} + q^n) \quad (7)$$

This decomposition is used to devise a hybrid iteration scheme, which recovers convergence or accelerates the convergence of diverging or slowly converging iterations, respectively. At each RPM iteration, only the projection of Eq. (1) onto  $\mathbb{Q}$  is solved with the standard fixed-point iteration, whereas the projection onto the typically low-dimensional invariant subspace  $\mathbb{P}$ , Eq. (7), is solved with Newton's method instead. Using the definitions of the projectors  $P$  and  $Q$ , Eq. (4), the RPM algorithm can then be written as:

$$p^{n+1} = p^n - V_p(V_p^T J^n V_p - I)^{-1} V_p^T (F(u^n) - u^n) \quad (8a)$$

$$q^{n+1} = F(u^n) - V_p(V_p^T F(u^n)) \quad (8b)$$

$$u^{n+1} = p^{n+1} + q^{n+1} \quad (8c)$$

where  $(V_p^T J^n V_p - I)$  is a small matrix of size  $k$ , whose inversion requires minimum computational effort. The Jacobian in Eq. (8a) is never formed explicitly, since it only occurs as a matrix-matrix product. It can be approximated with a finite difference scheme [130]: let the column vectors of  $V_p$  be  $v_j$ ,  $j = 1, \dots, k$ , then the matrix vectors product is given by

$$J^n v_j = \frac{1}{\varepsilon_j} (F(u^n + \varepsilon_j v_j) - F(u^n)) + \mathcal{O}(\varepsilon_j) + \mathcal{O}\left(\frac{\varepsilon_m}{\varepsilon_j}\right) \quad (9)$$

where  $\mathcal{O}(\varepsilon_j)$  is the truncation error and  $\varepsilon_m$  a measure for the floating point arithmetic accuracy.  $\varepsilon_j$  should be chosen such that the error terms are balanced. Stability analysis of the algorithm, Eq. (8), shows that its spectral radius is small then one, i.e., the scheme is stable [112].

The basis  $V_p$  is constructed and updated directly from the iterates  $q^n$  of the modified iteration (6c), without computing Jacobian matrices. This is done by monitoring

$k_s$  successive  $Q$ -projections of the residual  $\Delta q^n = QF(u^n) - q^n = q^{n+1} - q^n$ , which form an approximate Krylov subspace for the projected Jacobian  $QJQ$  [112]. Asymptotically, the Krylov subspace converges towards the dominant Eigenspace of  $QJQ$ . Every  $k_i \geq k_s$  iterations the Krylov subspace is used to compute the  $QR$  factorization

$$K = [\Delta q^{n-k_s+1}, \dots, \Delta q^n] = QR \quad (10)$$

where  $Q$  is an  $N \times k_s$  orthogonal matrix, and  $R$  is an  $k_s \times k_s$  upper triangular matrix. If the diagonal elements  $r_{i,i}$  of  $R$  satisfy

$$\left| \frac{r_{j,j}}{r_{j+1,j+1}} \right| > k_a, \quad 1 \leq j \leq k_s - 1 \quad (11)$$

for some  $j$ , where  $k_a$  is the Krylov acceptance ratio, the first  $j$  columns of  $Q$  are included in the new basis  $V_p$ . The Krylov acceptance ratio in Eq. 11 can be interpreted as a threshold for when  $K$  should be considered rank deficient, hence signaling when an approximate invariant subspace of dimension  $j$  is present [126]. This motivates the use of  $QR$  factorization with column pivoting to better determine the rank. The new basis has to be orthogonalized against the old basis,  $\widehat{V}_p$ , if present, by computing the  $QR$  factorization

$$V_p R = [\widehat{V}_p, Q_j] \quad (12)$$

Finally, the projected Jacobian is updated,

$$V_p^T J V_p = V_p^T J [\widehat{V}_p, Q_j] R^{-1} = V_p^T [\widehat{J\widehat{V}_p}, JQ_j] R^{-1} \quad (13)$$

The complete RPM algorithm is presented as pseudocode in Fig. 13. The theoretical properties of RPM are discussed in more detail in [112, 126].

#### 4.3.3. Implementation and Parallelization Issues

Here, the flow solver Edge, compare chapter 4.2, was interfaced with a Matlab implementation of RPM. RPM sends a vector  $u$  into the flow solver, which updates the boundary conditions and turbulent quantities, and returns  $F(u)$  after NSTEP iterations to the Matlab process, completing one RPM iteration. This is shown schematically in Fig. 14.

The Matlab process was synchronized with the Edge process by reading and writing a flag file (`elk.flag`) and a buffer file (`elk.buff`) containing the state vector  $u$  using the FFA Matlab Toolbox [131]. The i/o flow is handled by the Matlab routine `elk.m` and a corresponding Fortran90 routine, `elk.f`. The file exchange and synchronization is illustrated in the flow chart in Fig. 15.

The RPM parameters are specified in the main program, `RPM_script.m`. This routine initializes the RPM Matlab process and calls the routine `RPM.m`, which executes the actual algorithm, Eq. (8), and performs the basis identification according to Eq. (11). The routine `scale.m` scales the state vector, which it receives from

**Function**[ $u$ ] = RPM( $u, k_s, k_i, k_a, \text{max\_iter}, \text{tol}$ ):

```

set all counters to zero and initialize: basis.size=0; nr.K=0; check.K=0; nr.vectors.add=0;
N = size( $u, 1$ );  $V_p = []$ ;  $W = []$ ;  $K = \text{zeros}(N, k_s)$ ;
for  $i = 1 : \text{max\_iter}$  % main loop
     $F = \text{func}(u)$ ; % function evaluation of the flow solver's native Picard iteration scheme
    if basis.size == 0 % no old basis  $\hat{V}_p$  present
         $K(:, 2 : k_s) = K(:, 1 : k_s - 1)$ ;
         $K(:, 1) = F - u$ ; % add residual to approx. Krylov subspace, Eq. (10)
    else % old basis  $\hat{V}_p$  present
        Project solution:
         $q = u - V_p(V_p^T u)$ ;  $z = V_p^T u$ ; % introduce coordinate variable z
         $F_q = F - V_p(V_p^T F)$ ;  $F_z = V_p^T F$ ; % fixed point iteration, compare Eq. (8b)
        Newton step:
         $z = z + (I - V_p^T JV_p)^{-1}(F_z - z)$ ; % compare Eq. (8a)
        Update solution:
         $u = F_q + V_p z$ ; % compare Eq. (8c)
         $F = \text{func}(u)$ ;
        Update Krylov matrix:
         $K(:, 2 : k_s) = K(:, 1 : k_s - 1)$ ;  $K(:, 1) = F_q - q$ ;
    end if
    nr.K = min(nr.K + 1,  $k_s$ ); check.K = check.K + 1;
    if check.K  $\geq k_i$  and nr.K  $\geq k_s$ ;
        Do "economy size" QR-decomposition of  $K$  with column permutation  $E$ :  $KE = QR$ ;
        for  $t = 1 : k_s - 1$ ;
            if  $|R(t, t)| > k_a |R(t + 1, t + 1)|$ ; % check Krylov acceptance ratio, Eq. (11)
                nr.vector.add =  $t$ ; %  $t$  vectors will be added to  $V_p$ 
            end if
        end
        check.K = 0;
    end if
    if nr.vectors.add > 0 % if new basis identified
         $Q = Q(:, 1 : \text{nr.vectors.add})$ ;
        compute  $JQ$  using finite difference scheme, Eq. (9);
        add vectors to old basis,  $V_p = [V_p, Q]$ ;
         $W = [W, JQ]$ ;
        basis.size = basis.size + nr.vectors.add;
        Orthogonalize the new basis against the old, Eq. (12);
        Compute projected Jacobian  $V_p^T JV_p$ , see Eq. (13):  $W = WR^{-1}$ ,  $VJV = V^T W$ ;
        check.K = 0; nr.vectors.add = 0;
    end if
    if  $\|F - u\|_2 < \text{tol}$  % convergence criterion
        break
    end if
    Update old solution:  $u = F$ ;
end

```

Figure 13: RPM algorithm in pseudocode

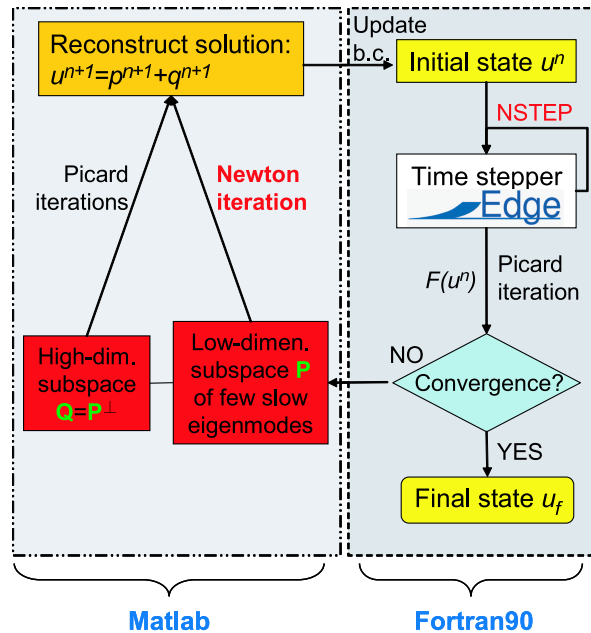


Figure 14: Schematic diagram of the Edge-Matlab implementation of RPM

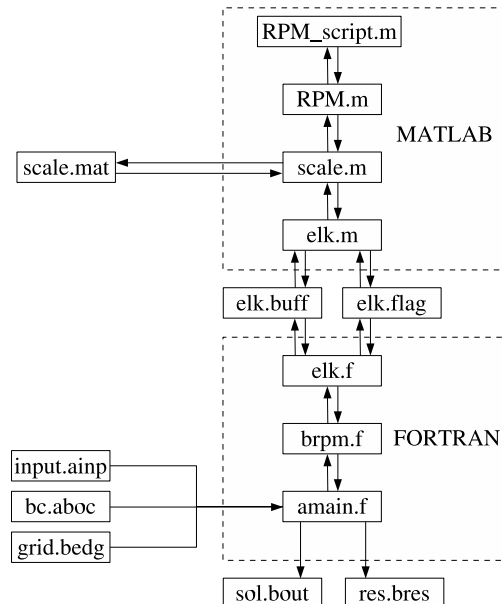


Figure 15: Flowchart of the file exchange and synchronization for coupling Edge to the Matlab implementation of RPM

or sends to the i/o routine `elk.m`, and writes the scaling parameters to the file `scale.mat`. The flow solver, on the other hand, sends its internal representation of the state vector to the routine `brpm.f`, which communicates with `elk.f` and updates the boundary conditions and turbulent quantities when an updated state vector is received from the RPM process. Edge reads the boundary conditions, the dual grid and the physical and numerical parameters from the files `input.ainp,bc.aboc` and `grid.bedg`, respectively, and writes the final solution and the convergence history to the files `sol.bout` and `res.bres`, respectively.

It was also important to take into account the magnitude of the different components of the state vector  $\mathbf{u} = (\rho, \mathbf{u}, \mathbf{v}, \mathbf{w}, p)^T$ , where  $\rho$  is the density,  $\mathbf{u}, \mathbf{v}, \mathbf{w}$  are the velocity components and  $p$  is the pressure. The components may differ in magnitude by several decades, depending on the choice of units, or scaling, of the variables. If the state vector is poorly scaled, the projections become easily perturbed, which can affect the performance of RPM. In [132] it is shown how the robustness of RPM is improved by proper scaling. In many models, some components, e.g. density, pressure and the turbulent kinetic energy, must stay positive. This can be guaranteed for explicit time-stepping schemes as long as the time step is sufficiently small, and the inherent dynamics of the model preserve positivity. For implicit methods with Newton linearizations and large time steps, there is no guarantee. Proper scaling of the variables improves robustness in this respect, too. However, there is no guarantee that RPM preserves positivity of the variables. A positivity scheme that damps the RPM correction to ensure that e.g. the turbulent kinetic energy stays positive can be a solution. However, such a scheme must be constructed such that it is consistent with the projections.

Significant elapsed time reductions via RPM can only be expected from a Fortran90 implementation of the algorithm into the flow solver. This is relatively straightforward because Fortran90 provides allocatable arrays, intrinsic matrix operations and so forth, very much like Matlab. The associated matrix factorizations (*QR* with column pivoting) can be computed by using LAPACK (Linear Algebra PACKage) [133].

Another key ingredient that is missing in the current implementation is parallelization. Distributing the RPM algorithm over many processors is not as straightforward. The efficiency of the algorithm strongly depends on the efficiency of the *QR* factorization with column pivoting, employed in Eq. (10), and the matrix inversion necessary in the Newton iteration, Eq. (8a). Efficient implementations of these operations are available in parallel linear algebra libraries for distributed memory computers like PLAPACK and ScALAPACK [134, 135]. PBLAS provides a global view of matrix operands, allowing global addressing of distribute matrices and ScALAPACK is a numerical linear algebra library for distributed-memory parallel computers. A BLAS-3 version of the *QR* factorization with column pivoting [136] will be employed, which outperforms the traditional BLAS-2 implementation both in serial and parallel architectures. This new version is available in LAPACK (version 3.0) as routine DGEQP3. Secondly, an inversion procedure based on Gauss-Jordan elimination could be used. This approach presents a better balance of the computational load for parallel distributed-memory architectures, see [137]. The use of these libraries enhances the reliability. The performance will depend on the efficiency of the underlying

serial and parallel computational linear algebra libraries and the communication routines, such as BLACS (Basic Linear Algebra Communication Subprograms, which is the MPI based communication layer of ScALAPACK), as the resulting inter-processor data traffic will slow down the effective solution rate.

## 5. Pre- and Postprocessing

A typical numerical flow simulation in CFD generally consists of the following three major steps [3]:

1. acquire the geometry and generate a numerical grid (preprocessing),
2. run the flow solver,
3. extract and process engineering data from flow-solver output (postprocessing).

The first step, i.e. acquiring geometry from a CAD system and generating a grid on it, has been one of the major bottlenecks in this study and deserves some closer attention. The second step, the actual numerical simulation, is discussed in length in the appended papers and will not be treated here. Finally, the post-processing step, which is very labor and CPU intensive when unsteady data is to be analyzed, will also be discussed and some novel post- and co-processing tools will be presented.

### 5.1. Preprocessing

All the steps required to create the input to the flow solver NSMB are illustrated in Fig. 16. First, the delta-wing geometry has to be modeled in a Computer Aided Design (CAD) environment. DDN, the CAD tool coming along with the commercial grid generation system ICEM CFD, was used for this purpose. DDN saves the CAD data in a so-called *tetin* file, which can be read by any of the grid generation tools of ICEM CFD.

Then, a structured numerical grid is constructed to enclose the boundaries of the delta wing in the flow field using the grid-generation tool ICEM CFD Hexa. This versatile grid generation tool is based on a global block topology and provides a top-down approach to grid generation. It is this top-down approach that significantly complicates the grid generation process, because finding a suitable blocking strategy requires a great deal of ingenuity, creating it is then easily done assuming a great deal of previous blocking experience. The blocking has to be done manually by splitting the super-block into a number of smaller blocks. O-type grids, however, can be generated by the system automatically in specified parent blocks. The blocking for a sharp delta wing is especially demanding because its apex is a geometric singularity and one faces the choice to either create a simple blocking with an undesirable grid singularity or to find a blocking that will avoid the creation of a singularity. The high leading-edge sweep angle sets the smallest angle of the cells at the apex, making them rather skewed. It can be concluded here that in spite of considerable advances in grid-generation techniques, constructing structured grids on a delta wing, or, even worse, a complete aircraft geometry, continues to be a labor-intensive and time-consuming

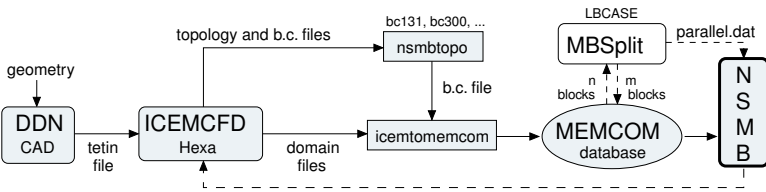


Figure 16: Preprocessing steps required to create database for flow solver

task, compare also [3] e.g.. The quality of the first grid is usually not satisfactory. Either the flow solver fails to converge on it or the grid is unable to resolve key flow features [3]. Rework is thus almost always required to improve grid quality. This is illustrated by the dashed-line going from the flow solver to the grid- generation tool in Fig. 16.

Once the blocking is generated, the grid point distribution has to be specified and optimized to suit the intended type of flow simulation, i.e. either an Euler simulation or a Navier-Stokes simulation. In this step one also has to take into consideration if the grid has to be multigrid capable or not. Compared to unstructured grids the disadvantage of structured Navier-Stokes grids is that i) their generation is more difficult and more time-consuming, ii) the layers of boundary cells have to be extended all the way to the far-field boundaries, resulting in an unnecessary large number of grid cells in regions of slowly changing flow quantities.

The final step in the grid generation process is to improve the grid metrics by applying some smoothing algorithm. This step has usually been omitted in this study because the smoothing algorithms in ICEM CFD proved to be very time consuming and did not result in grid orthogonality at the walls.

The output of the grid generation system is a number of so-called domain files, which contain the coordinates of the grid point in each block, and files that describe the connectivity between the different blocks. Before these files can be assembled to a database that can be read by NSMB, the boundary conditions have to be specified and written to a file using the interactive program `nsmbtopo`. It reads and interprets the topology and boundary condition files generated by ICEM CFD Hexa. Next, the utility program "`icemtomemcom`" reads the topology file with boundary condition information created by `nsmbtopo` together with the domain files generated with ICEM CFD Hexa, and creates the MEM-COM database.

The database can then be used perform the actual numerical simulation. Usually, however, the grid with  $n$  blocks has to be split again, typically resulting in more blocks  $m$ , to achieve good load balance on a parallel high-performance computer. The load-balancing tool MB-Split is used for this purpose. It reads the MEM-COM database and an additional file, `LBCASE`, which contains processor timing information and the number of processors, splits the blocks and distributes them in a suitable way on the processors. The block assignment to processors is saved in the file `parallel.dat`. The split database can be written to a new MEM-COM database. During this thesis, it was discovered that MB-Split does not fully support multigrid. It can happen that it performs a split that results in a block that has only five grid point in one direction,

which corresponds to four cells. The maximum number of multigrid levels for such a grid would be two. Multigrid, however, usually employs three (or more) grid levels, which would result in only one cell

## 5.2. Scientific Visualization of Steady and Unsteady Flow-Field Data

The computation of steady turbulent flow is common practice in industry today. Unsteady simulations, however, are still considered challenging in terms of CPU and memory requirements. Data storage and processing is also an issue, because unsteady calculations often generate several hundred or thousand time steps. Each time step may require tens or hundreds of megabytes of disk storage, and the entire unsteady flow data set may be hundreds of gigabytes. The visualization of unsteady flow fields data is not straight forward either, and the extraction of flow features, such as vortex cores, or the animation of pathlines are very CPU intensive.

### 5.2.1. Data Storage and Visualization Approach

The unsteady solution can be stored and processed in different ways. The common approach for *steady* data is to save the flow field variables at each grid point to the MEM-COM database, which also contains the grid and boundary condition information. The data is saved in binary format in so-called data sets. *Unsteady* data can be saved to the database in very much the same way at specified time intervals, although every time step has to be written to a different data set. This is done in NSMB by automatically increasing the data set number. The database, which is an ordinary Unix file, gets very large after only a few time steps. Handling such a large file is very inconvenient, especially if they have to be transferred by `ftp` from the computing facility to the visualization environment.

Recognizing this dilemma, Le Moigne [17] suggested an alternative approach. Instead of saving the entire flow field, he performed the visualization before saving to disk, i.e. while the calculation was still running, effectively co-processing simulation and visualization. In this approach the visualization has to be automated. The commercial flow visualization software EnSight was coupled to NSMB and instructed to probe the flow field according to previously specified criteria or for flow features, such as cortex cores. Only the required data is extracted from the solution this way and then saved to disk. The rest of the data at this time step is discarded, with the consequence that it cannot be visualized again at a later time. Thus, one has to know *a priori* what kind of flow features to expect, which might not always be the case. Another computation might become necessary if something was missed.

Here, a third approach is pursued. The entire flow solution is written to a file in `plot3d`-format at specified intervals. Every new solution is written to a different file. Only the last time step is saved to the database, enabling a continuation of the calculation at a later time. The solution files are typically on the order of tens of megabytes and can easily be transferred by `ftp`. To save disk space on the high-performance computer, files are migrated to a mass storage system from time to time while the computation is running. Selected files can be transferred directly to the visualization environment or fetched from the mass-storage system at a later time.

This reduces the local storage requirements on both the high-performance and the visualization computer. This approach is illustrated in Fig. 17.

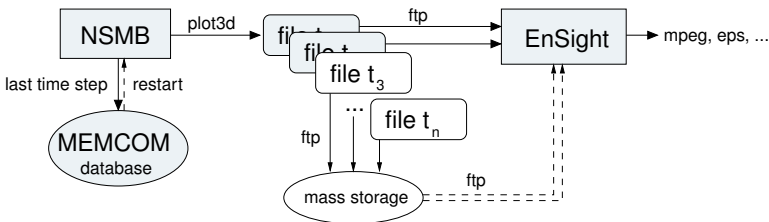


Figure 17: Data storage and visualization approach

### 5.2.2. Visualizing Transient Data

Streamlines<sup>3</sup>, contour lines, vector plots, and volume slices (cutting planes) are commonly used for flow visualization. These techniques are sometimes referred to as instantaneous flow visualization techniques because calculations are based on an instant of the flow field in time.

Although instantaneous flow visualization techniques are effective for depicting phenomena in steady flows, they sometimes do not adequately depict time-varying phenomena in unsteady flows. Streaklines and timelines are effective visualization techniques for depicting vortex shedding and vortex breakdown in unsteady flows [138]. These techniques are examples of time-dependent flow visualization techniques, which are based on many instants of the flow fields in time. A *streakline* is a curve formed by all particles that were previously injected from a fixed location. A *timeline* is a curve formed by all particles that were injected simultaneously at some instant in time from a set of fixed seed locations. Both of these techniques trace particles through many time steps of the given unsteady flow data.

In experimental flow visualization, the behavior of the flow is analyzed by continuously injecting smoke or dye into the flow from some fixed seed locations. The smoke or dye is then photographed after some time has elapsed. If the flow is steady, then the smoke patterns photographed are streamlines. In numerical flow simulations, the flow data are saved only at discrete points in time and space. To simulate streaklines, small massless particles are injected into the flow from several seed locations at each saved time step. The particles are then traced both spatially and temporally. In EnSight, streaklines are displayed by animating pathlines generated with emitters emitting at multiple time intervals. A *pathline* is the trajectory of a particular fluid particle. It is different for different fluid particles. In steady flows pathlines are streamlines. The pathlines are particle traces and are created in EnSight by integrating the vector field variable over time using a forth-order Runge-Kutta method and utilizing a time varying integration step [139]. The integration step is lengthened or shortened depending

<sup>3</sup>A streamline is a curve whose tangent at any point is in the direction of the velocity vector at that point. If the flow is unsteady the streamline is different at different times as the velocity vectors are fluctuating with time

on the flow field. One has the choice between massless or massed particles. In the present study only massless particles are traced.

When comparing experimental streaklines with the numerical streaklines generated in EnSight, experimental streaklines are usually smooth and continuous, whereas numerical streaklines are represented by discrete points. This is because particles are injected continuously in experimental flow; however, in numerical flows, particles are injected at discrete time steps. The time resolution of the numerical flow dictates how continuous the streaklines appear. Unfortunately, most large 3D unsteady flow simulations are saved at a coarse resolution, for example, at every 50th or 100th time step due to disk limitation. Hence, numerical streaklines may not always be smooth. For this reason, numerical streaklines usually are not connected because they can be jagged. Nevertheless, numerical streaklines still can reveal features that are visible in experimental streaklines. Here, streaklines were generated to investigate if spiral or bubble-type breakdown is predicted by the numerical scheme and how the post-breakdown flow region evolves with time. Note that the placement of the seed points of the streaklines is critical in obtaining a good depiction of the flow. Here, several particles were released along a line coinciding with the vortex axis upstream of the point of vortex breakdown.

### 5.2.3. Oil-Flow Patterns

Oil-flow patterns were created by computing skin-friction lines on the wall surface of the model. In EnSight this is done by computing surface restricted streamlines. The streamlines will be constrained to stay on the surface of the selected model parts by using only the tangential component of velocity.

### 5.2.4. Vortex Cores and Vortex Breakdown

A very powerful way of analyzing a vortical flow field is by looking at the spatial and temporal development of vortex cores. Vortex cores are at the center of swirling flow. Vortex cores also reveal vortex burst. It is characterized by a kink in the vortex core filament [42].

The feature-extraction tool was not yet available in EnSight at the time of the writing of the first two appended papers. Vortex cores were instead extracted “by hand” by releasing a streamline close to the delta wing apex, which was traced both upstream and downstream of the seed point. This streamline was typically following a helical paths around the axis of the vortex. The core was then found by interactively repositioning the seed point until the streamline was a straight line starting at the apex. At the point of vortex breakdown, this straight line would start to kink out and spiral. Flow quantities, like the axial component of velocity, were then extracted along this “vortex-core streamline”. Sometimes it was not possible to trace the exact location of the vortex core. The streamline was then still spiraling somewhat around the true vortex core axis. This is the reason for the “wavy ness” in the axial velocity along the vortex core axis in Fig. 12 and 20 of Paper A, e.g. An improved extraction method was then devised for all other figures. Instead of extracting the flow quantities along the spiraling streamline they were extracted along a straight line tool, which was placed

in the flow field such that it would start at the apex and follow the axis of the slightly spiralling streamline.

For Paper C, the automatic feature-extraction functionality of EnSight was used instead. EnSight creates vortex core segments from the velocity gradient tensor, which is computed for each node in the grid. The first of the two available extraction algorithm uses classification of Eigen-values and vectors to determine whether a vortex core intersects any face of a grid cell. The vorticity based algorithm utilized the fact of alignment of the vorticity and velocity vectors to determine core intersection points [139]. The problem with the linear implementation of the two vortex core extraction algorithms in Ensight is that both have problems finding cores of curved vortices. This is especially true downstream of the point of vortex breakdown, where the core spirals in a corkscrew-like fashion. The resulting vortex core is rather segmented and discontinuous in the breakdown region. The algorithms are also not very good in predicting core segments of weak vortices, such as the secondary or higher-order vortices over a delta wing. Also, due to the difference in algorithms, some segments produced may not be vortex cores. Some qualified judgement by the user is needed to identify such “unphysical vortex cores”. In EnSight, such segments can be filtered out according to different variables via thresholding options.

### 5.2.5. Vortex Breakdown Criteria

There is considerable scatter in experimentally measured breakdown locations for a wing of a given sweep angle and incidence. On one hand “it is difficult to measure the same [breakdown] point repeatedly” [140], since it can oscillate along the axis of the vortices and it is as well not a sharply defined location. On the other hand, breakdown is influenced by far more parameters than wing-sweep angle and incidence and cannot be defined using only local quantities [28]. Breakdown rather depends on the history of the vortex before entering the breakdown region, the entire shape of the axial and swirl velocity profiles and the shape of the axial pressure distribution – this makes it difficult to find a unique breakdown criterion.

Important information on the burst location can be obtained by analyzing the flow field by visual means. This has been and still is a common practice in experimental investigations. In surface oil patterns breakdown is indicated by a kink on the secondary separation line [42]. This criterion cannot be applied in a numerical simulation unless a transition model is applied. Another criterion is a kink in the vortex core filament, as was mentioned earlier. Here, the breakdown location was defined as the chordwise location closest to the wing apex where the chordwise component of the velocity  $u$  along the vortex core axis equals zero. This is in line with the experimental finding that on the vortex axis the axial component of the velocity is increasing up to the breakdown location where it decreases abruptly [28, 35–37]. Another useful criterion is based on vorticity. Özgören *et al* [141] found experimentally that a switch in sign of azimuthal vorticity precedes the occurrence of a stagnation point at the leading portion of bubble-type breakdown. This observation is in accordance with the theoretical finding of Brown and Lopez [142] that a zero or negative velocity along the vortex axis can only occur when the azimuthal vorticity becomes negative. The last

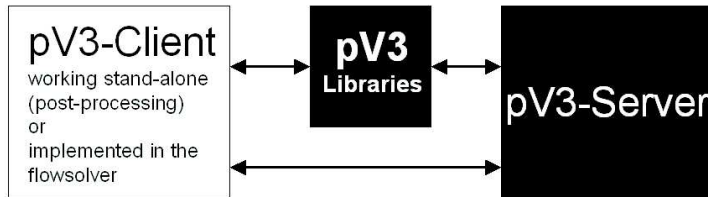


Figure 18: The three parts of pV3

two criteria are compared in Paper A. They result in practically the same breakdown location.

Many alternative criteria have been suggested, among them those based on a unique number, e.g. the swirl ratio or Rossby number. The definition of a vortex breakdown criterion by a unique number or a single curve in the plane of two variables is, however, “a big oversimplification of reality” [28].

### 5.3. Co-Processing Visualization with pV3

Co-processing visualization of CFD-data has two major advantages over post-processing visualization. It is possible to look at the data as it changes (convergence) and the user may notice inconsistencies in the intermediate results and decide to terminate the flow computation.

Here, co-processing visualization was done by linking the flow solver Edge, compare chapter 4.2, to pV3. pV3 (parallel Visual3) [143–145] is a distributed system that has been designed specifically for co-processing visualization of data generated in a distributed and parallel computing environment. It is also designed to allow the solver to run as independently as possible. pV3 can “plug” into the flow computation at an arbitrary point in time and requires computing resources only during the visualization session. It has been developed at the Department of Aeronautics and Astronautics at MIT (Massachusetts Institute of Technology) and is an extension of the serial visualization software Visual3 [146]. The compiled source code is freely available for several operating systems. PVM<sup>4</sup> [147] and OpenGL are required, as well as specific compilers on some platforms.

pV3 consists of three elements, as shown in Fig. 18. The basic element of pV3 is a collection of libraries, which are not executable by themselves. The pV3-Client [148] is the element that supplies pV3 with data and has to be adapted to the user’s specific visualization requirements. The client is a Fortran program that has to be implemented into the flow solver unless a stand-alone post-processing tool is required. By calling a set of routines provided with the pV3 libraries, the client initializes pV3 and provides it with information about the grid, the cells and the boundaries. After this first calling sequence, the pV3 Server can be launched as

---

<sup>4</sup>PVM (parallel virtual machine) from Oak Ridge National Laboratory is public domain communication software that transforms a (heterogeneous) network of machines into one *virtual* parallel computer.

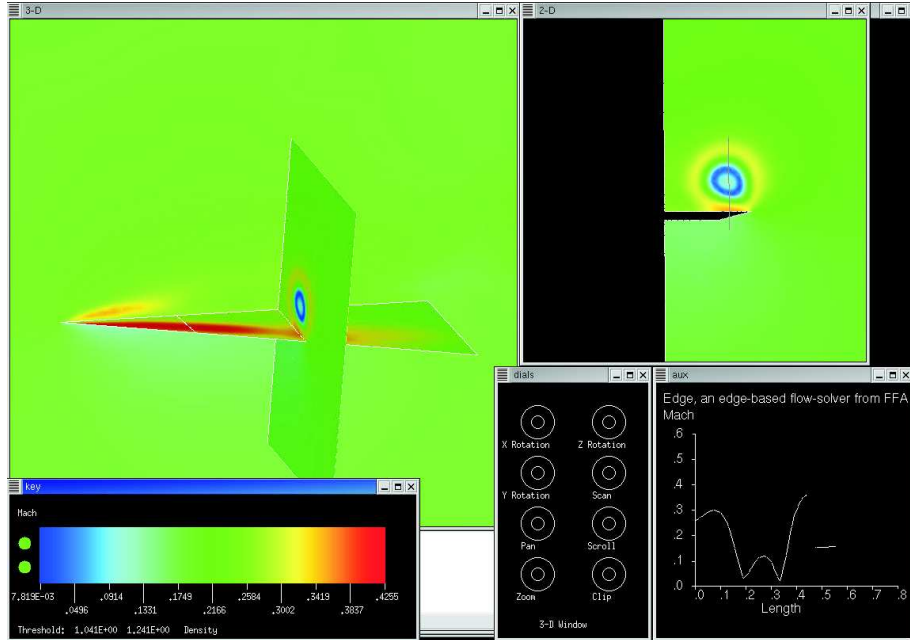


Figure 19: Screenshot of pV3 Server showing a post-processing visualization example

long as a client is running. This interactive server [149] is the third element of pV3 and represents the graphical user interface (GUI). After starting the server, the second part of the calling sequence begins and the client provides the server with scalar and vector data. In the case of post-processing visualization, this is done every time the user changes the variable to be displayed. In the case of co-processing, the client sends a message to the server (if it is running) to update its data every time a new new solution is available. A screenshot of the pV3 Server is shown in Fig. 19.

In a first step, a stand-alone post-processing visualization tool based on pV3 was developed. This tool reads Edge grid and solutions files in FFA format, the native Edge format. No file conversion is needed. It can handle both structured, unstructured and hybrid grids, based on any kind of simple cells.

The next logical step was the implementation of a pV3-Client into the serial version of Edge for co-processing visualization of CFD-data in serial mode. For this purpose it was necessary to implement both the initialization part and the update part of the pV3 Client into the Edge main routine. The initialization client was implemented before the main iteration loop. It reads the primary grid information from the grid file in FFA format, because this information is not explicitly stored in the Edge data structure (only the dual grid is stored). The update client, on the other hand, extract the scalar and vector data from the internal data structure and sends it to the pV3 Server after each update call. It was implemented into the inner iteration loop. Consequently, it is only possible to visualize the inner-loop convergence of every physical

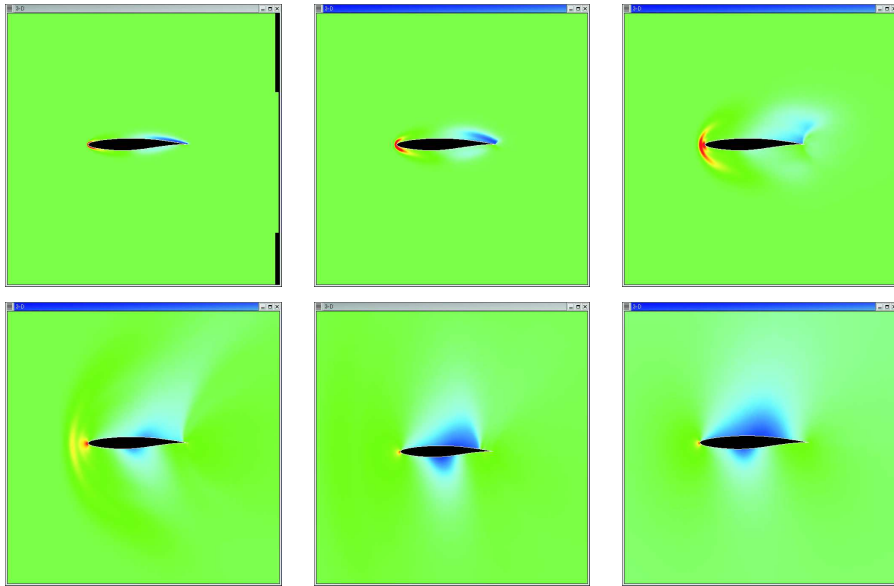


Figure 20: Visualization of intermediate solutions after 10, 25, 50, 100, 200 and 1820 iterations (converged solution) with co-processing visualization tool

(outer) time-step of an implicit time-accurate simulation (dual time stepping). The visualization of an unsteady flow solution, which would require the update client to be placed outside the inner iteration loop, was considered not feasible because it may require tens or even hundreds of iterations to converge the inner loop of dual time stepping. Potentially, this could translate into very long delays between two server updates.

It would be possible to circumvent this problem by employing the pV3 Batch Server [150] instead, which is designed for use with time-accurate flow problems. It automatically extracts flow-field data from intermediate solutions while the flow solver is running. The saved solutions can then be visualized in post-processing mode. The major advantage is that the pV3 Batch Server only extracts the data of interest (must be defined before). The batch server can also be combined with the Fluid Feature Extraction tool kit FX [151], which automatically detects shocks, vortices and separation.

The developed co-processing visualization tool makes it possible to look at intermediate results while Edge is running. The serial implementation has been tested and validated on simple test-cases with structured and unstructured non-moving grids, such as the flow around an airfoil and a delta wing. In Fig. 20, intermediate results computed for a NACA-airfoil at  $M_\infty = 0.73$  and an angle of attack of  $2.8^\circ$  (Euler-calculation) are visualized in serial co-processing mode with pV3. The figure show clearly how the solution converges.

In a last step, parallel co-processing visualization was experimented with. Before a flow problem can be calculated on a parallel computer, the Edge preprocessor has to

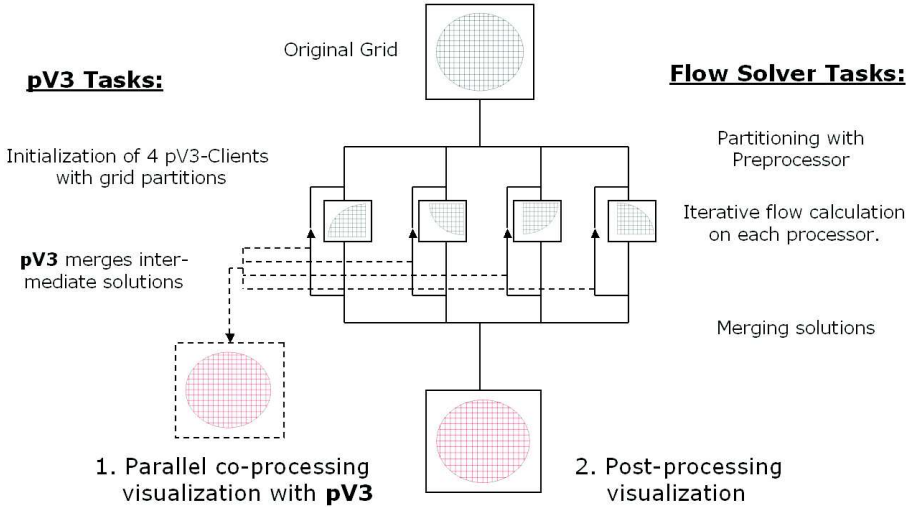


Figure 21: Parallel co-processing visualization of CFD data with pV3

divide the original grid into several partitions matching the number of processors to be used. This is illustrated for four partitions in Fig 21. During the parallel computation, pV3 has to be initialized by launching one pV3 Client on each processor. Each pV3 Client only sends the grid information of its own partition to pV3. When a visualization session is started by launching the pV3 Server, the update-part of each client provides its current solution. pV3 collects all solutions using PVM and merges them to an intermediate solution of the flow problem, which is then displayed with the pV3 Server.

Unfortunately, it was not possible to implement this parallel visualization model into Edge, because the flow calculations in Edge are based on the dual grid, which is generated and then partitioned by the preprocessor. The primary grid information, which is mandatory for the initialization of pV3, is lost in this process and cannot be reconstructed for the individual grid partitions. Consequently, it is not possible to initialize pV3 correctly. Major modifications to the preprocessor would be required to retain or reconstruct this information. Nevertheless, the modifications required for parallel co-processing visualization have been made to the pV3 client in Edge, assuming that primary grid information is available for each partition.

More details on the implementation of pV3 in Edge can be found in [152].

## 6. Summary of Appended Papers

In the following, some of the main results of the appended papers are lifted out and supplemented with some new or additional results.

### Paper A

The first paper maps out the research area of vortex breakdown and looks at the entire flight envelope for delta wings. A *semi-span* sharp leading- and trailing-edge  $70^\circ$  delta wing was selected for analysis based on an extensive literature survey [153] on experimental and numerical investigations of delta wings. Good aerodynamic coefficient and vortex breakdown location data was available for this wing from experiments by Soltani and Bragg [51, 154, 155]. The literature survey also demonstrated that there are few publications of comprehensive wind-tunnel tests where all data was measured under the same flow conditions. Another reason for selecting a flat-plate delta wing was to study a model problem that contains only generic aspects of vortex flow in a simple setting, keeping the numerical simulation free of other complications.

Steady-state calculations at different angles attack ranging from  $10^\circ$  to  $40^\circ$  were performed. Inviscid, laminar and turbulent solutions were computed on a *single viscous* grid to assess the role of viscosity in the breakdown process. The breakdown location was seen to be quasi-steady and practically independent of physical modeling. Good agreement with experimental data is seen in Fig. 22.

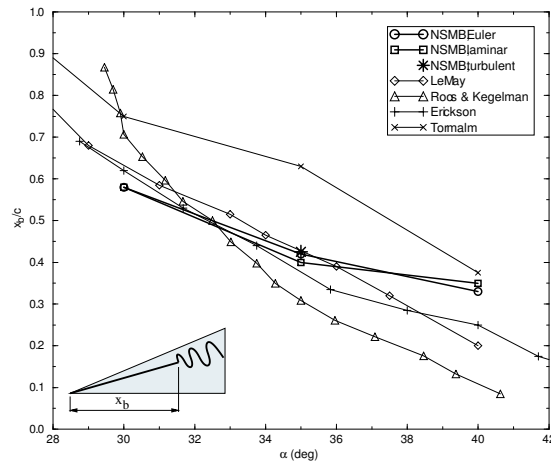


Figure 22: Computed vortex breakdown locations compared to experimental data [36, 156–158] ( $M_\infty = 0.16$ ,  $Re = 1.97 \times 10^6$ , different physical modeling)

### Paper B

The second paper deals with aspects of grid generation, numerical parameters and non-linear vortex interaction over a delta-wing/body model. It was demonstrated that

the grid generation process plays an important role in the simulation of the aerodynamics of delta wings at high angle of attack. The advantages and disadvantages of several grid types were discussed. A H-H type topology was shown to be most suitable for the numerical simulation of sharp-edged delta wings. This finding was supported by additional grid studies by Malmlöf [159]. Details of the flow field were shown to be highly dependent on grid topology and grid fineness at the apex, the leading edge and in the vortical flow region over the wing. An embedded-conical type grid proved not to be suitable for the simulation of the high-alpha aerodynamics of delta wings, because it produced unphysical solutions for the flow quantities in the vortex core. In particular the axial variation of velocity along the vortex core axis was seen to be unphysical for this grid type. The supposedly correct axial velocity profile was computed on a fine H-H type grid without singularity at the apex. Artificial dissipation was shown to influence the damping of the rotating breakdown region.

Note that the delta-wing geometry of Soltani and Bragg was abandoned after the first paper because i) no surface pressure measurements were taken in their experiments, making a comprehensive comparison between computed and experimental data impossible, and ii) the upper surface bevel complicated the flow field and grid generation unnecessarily. The extensive wind-tunnel data published by Kegelman and Roos [36, 37, 47, 160] made me adopt their  $70^\circ$  *semi-span* delta wing instead. The discrepancy between the computed and experimental upper surface pressure distribution reported in Fig. 20 in Paper B was later traced back [161] to excessive blockage effects in the experiments of Kegelman and Roos. They tested the semi-span delta wing model with a root chord length of 762 mm and a semi-span of 277 mm in a test section 910 mm wide and 740 mm high but failed to report any estimation of the size of the blockage effect. The presence of the tunnel walls confining the flow around a model in the test section reduces the area through which the air must flow as compared to the free-air conditions simulated in the computation and hence, by continuity and Bernoulli's equation, increases the velocity of the air as it flows in the vicinity of the model [162]. The blockage effect is to reduce the surface pressure, as can easily be seen in the attached flow region close to the root of the semi-span wing in Fig. 20. It was therefore concluded that future comparisons should not be based on the data by Kegelman and Roos.

**Delta-Wing/Body Model:** With a more realistic configuration in mind, a delta-wing/body model was studied experimentally in the L2000 wind tunnel at KTH and computationally using NSMB. The flow was anticipated to be more complex because of round leading edges (smooth-surface separation), the presence of a fore and center body (vortex interaction), and a blunt base (base vortices).

In the experiment a single column of smoke was introduced upstream of the model and positioned so that it would impinge on the forebody apex. The smoke then became entrained into the body and wing vortices making them visible. Several interesting observations were made. At moderate angles of attack, no body vortex could be observed. The wing vortices were intact. At higher angles of attack, the wing vortices were observed to break down, with breakdown moving more upstream with increasing angle of attack. Between  $30^\circ$  and  $35^\circ$  angle of attack, strong body vortices were observed to interact with the broken down wing vortices. The interaction is shown in Fig. 23(a) for  $35^\circ$  and compared to flow field visualization of numerical results at

slightly different flow conditions in Fig. 23(b) (the Mach number was increased in the fully turbulent numerical simulation to avoid numerical problems). The numerical

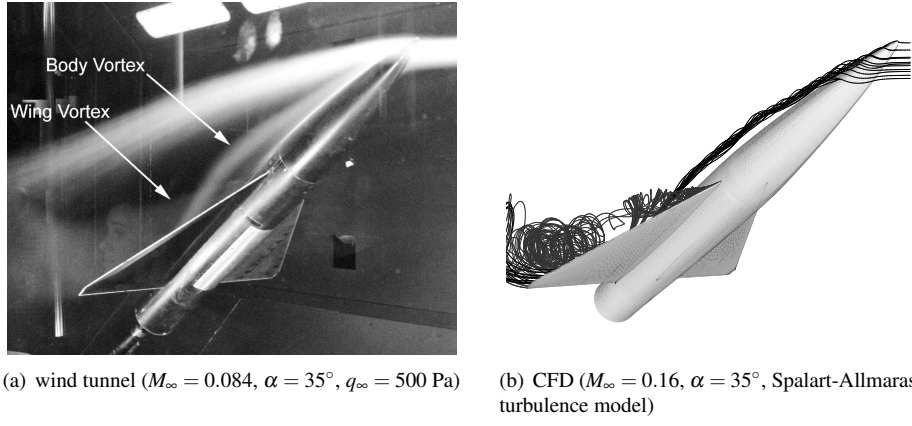


Figure 23: Vortex interaction over generic delta-wing/body compared

scheme captured both the forebody vortex and the burst wing vortex and their mutual interaction. The body vortices were seen to be asymmetric in the experiment, with the port body vortex lying above the starboard body vortex. This could not be captured by the simulation because only a *semi-span* model was simulated to reduce the computational cost. Additional flow features computed off-surface are visualized in Fig. 24. Vortex cores were extracted from the solution and used to seed the flow field with streamlines. A secondary forebody vortex core is observed underneath the primary forebody vortex core. Both cores are seen to interact with the wing vortex. Even a tertiary vortex core is captured for some distance. Over the wing, a burst primary vortex is observed. Nevertheless, the global circulatory flow pattern still exists over the wing, as is indicated by the spiraling streamlines. Also notice a vortex in the corner between the wing and the center body. This corner vortex will be discussed in more detail a little later. A base vortex is located behind the blunt base of the center body. Figure 25 presents computed surface skin frictions lines on the model, revealing the influence of the forebody and wing vortices on the surface of the model. The skin-friction lines close to the nose of the forebody are seen to flow towards the primary separation line from both sides where they lift off the surface to form the primary forebody vortex. The primary separation line is seen to start somewhat downstream of the apex and terminates some distance downstream of the wing apex. Looking at the body from the nose in the downstream direction and seeing the circular cross-section as a clock face, the primary separation line is at about the two o'clock position. The primary attachment line is located at the twelve o'clock position on the forebody. A secondary separation line can be seen to start at about half the distance between the nose of the body and the apex of the wing. It is located at about the one o'clock position and terminates some distance downstream of the point where the primary separation line disappears. This confirms the existence of a secondary vortex underneath the primary forebody vortex. The interaction of the primary and secondary body vortices with the

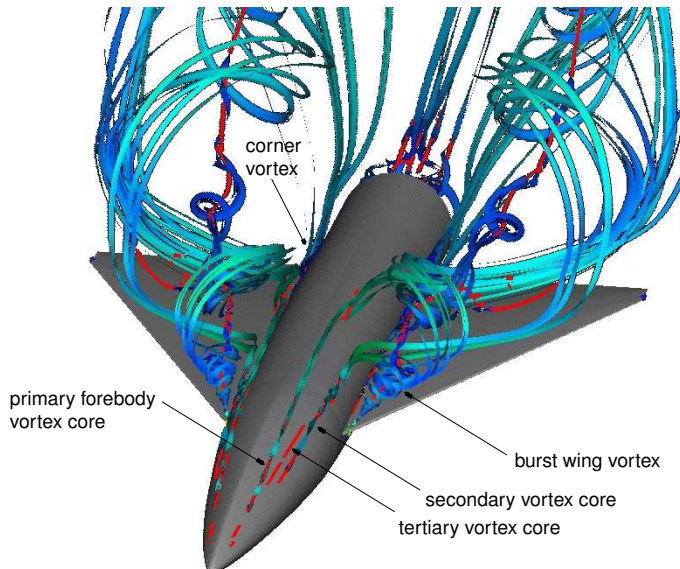


Figure 24: Vortex breakdown and vortex interaction over generic delta wing-body model ( $M_\infty = 0.16$ ,  $\alpha = 35^\circ$ , 1-eq. turbulence model)

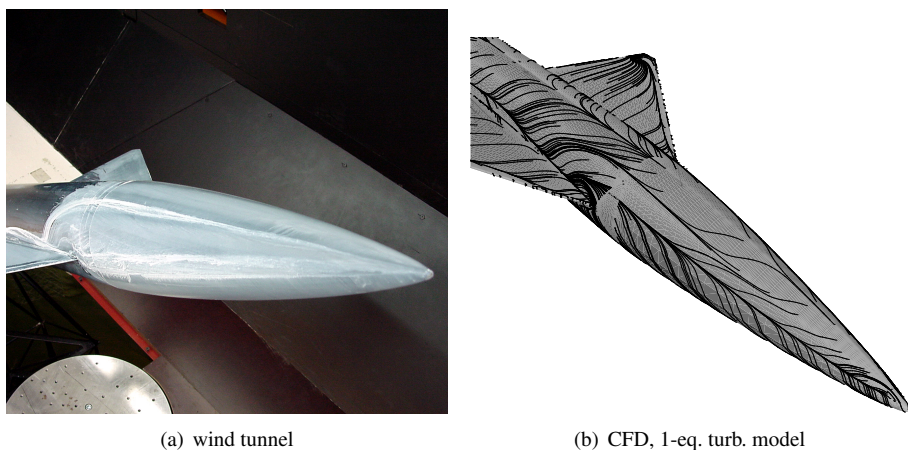


Figure 25: Computed skin friction lines on wing-body model compared to experimental oil-flow pattern ( $\alpha = 30^\circ$ )

wing vortices can clearly be seen from the primary and secondary separation lines on the forebody, which turn downward towards the wing downstream of the wing's apex. Another interesting observation is made in Fig. 26, which shows the skin friction lines on the cropped delta wing, seen from above. The secondary separation line is seen to

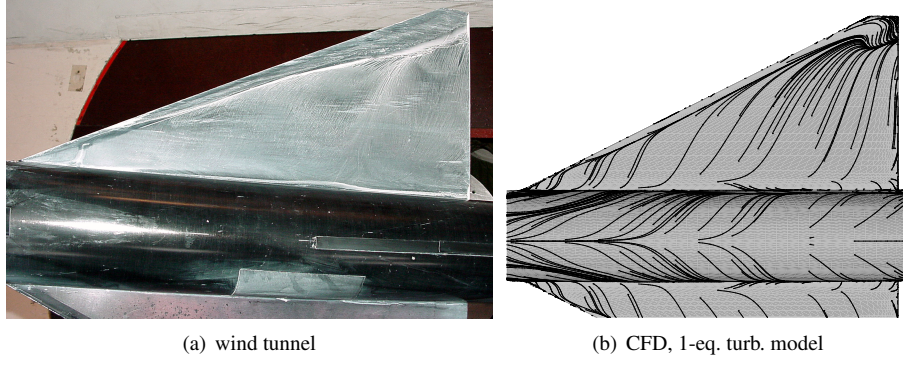


Figure 26: Computed skin friction lines on cropped delta wing compared to experimental oil-flow pattern ( $\alpha = 30^\circ$ )

bend inboard close to the cropped wing tip. A very similar flow pattern was observed over a sharp delta wing with a convex upper surface by Earnshaw and Lawford [55], among others. The pattern indicates a “focus-type” separation [1], in which the separated boundary layer on the lee side of the wing rolls up into a “tornado-type” vortex stem. This is illustrated in Fig. 10 for a pure delta wing. In Earnshaw and Lawford’s experiments, this pattern appeared at high incidence and was always a feature of transition from a “vortex-type” surface flow pattern to the complete flow reversal associated with the bluff-body wake occurring at even higher incidence. In the present case, the incidence angle is close to that corresponding to maximum lift with vortex breakdown close to the apex. The computed skin friction lines outboard of the secondary separation line suggest flow reversal occurring at the tip of the trailing edge. Also note the attachment line on the wing close to the center body with a corresponding separation line on the center body in Fig. 25. The rather large center body actually defines a corner-type flow. The interaction between the rolled-up leading-edge vortex and the corner flow near the body causes the appearance of a secondary vortex. Obviously, the flow field is significantly more complex than that over a “clean” delta wing.

### Paper C

The third paper deals with another important aspect of vortex breakdown, its inherent unsteadiness at high stationary angles of attack. It was decided that the *full-span*  $70^\circ$  delta wing studied experimentally by Mitchell [24, 39] was best suited for this purpose. This test case was also adopted for validation and verification of CFD computations by the NATO Research and Technology Organization (RTO) Applied Vehicle Technology (AVT) task group AVT-080 “Vortex Breakdown over Slender Wings,” in which

I have been a member. Mitchell measured the time history of the port and starboard vortex breakdown location, the upper surface pressure distribution, the upper surface oil flow pattern, and in planes normal to the wing upper surface the distribution of i) the different velocity components, ii) the axial vorticity component, iii) the turbulent kinetic energy, and in a longitudinal plane through the vortex axis the distribution of a) the different velocity component, b) the azimuthal vorticity component, and c) the turbulent kinetic energy.

Inviscid calculations were preformed on an Euler-type grid for three angles of attack using explicit global Runge-Kutta time stepping. Despite symmetric boundary conditions the numerical solutions were seen to exhibit asymmetry in the port and starboard vortex breakdown locations, as well as streamwise oscillations of the breakdown location. Flow visualization revealed that spiral-type breakdown was predicted over both sides of the wing. The rotation of the port and starboard post-breakdown helical structures was shown to be out of phase. Intermittent bubble-type breakdown was also observed to occur periodically over one side or the other of the wing and related to the occurrence of asymmetry in the breakdown location. The temporal evolution of the aerodynamic coefficients was analyzed by means of spectral analysis, revealing the helical mode instability (spiral-type breakdown) as well as fluctuations of the breakdown location. Figure 27 presents the normal force coefficient as a function of time for the time-accurate Euler simulations of the full-span wing, demonstrating the different nature of the flow field at different angles of attack.

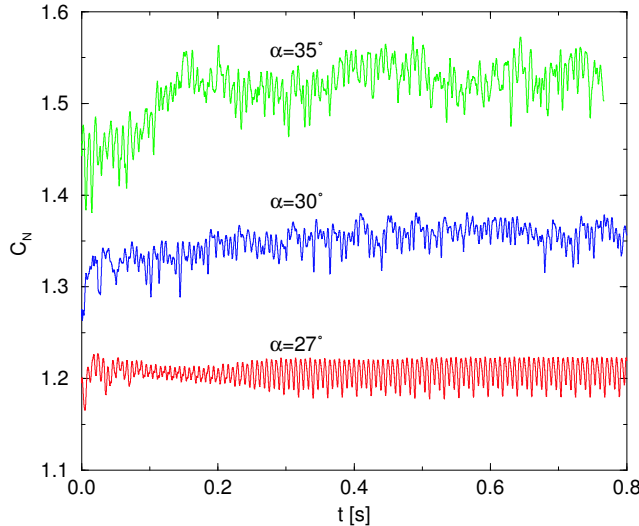


Figure 27: Normal force coefficient vs. time for different angles of attack ( $M_\infty = 0.2$ , Euler)

At  $\alpha = 27^\circ$  the normal force coefficient oscillates harmonically after some initial transients. This is due to the spiral-type breakdown rotating in phase over the left and right wing and the breakdown location being symmetric and stable. At  $\alpha = 30^\circ$  and  $35^\circ$ ,

however, low frequency oscillations due to the streamwise movement of the breakdown location and its asymmetry are superimposed on the high-frequency oscillation.

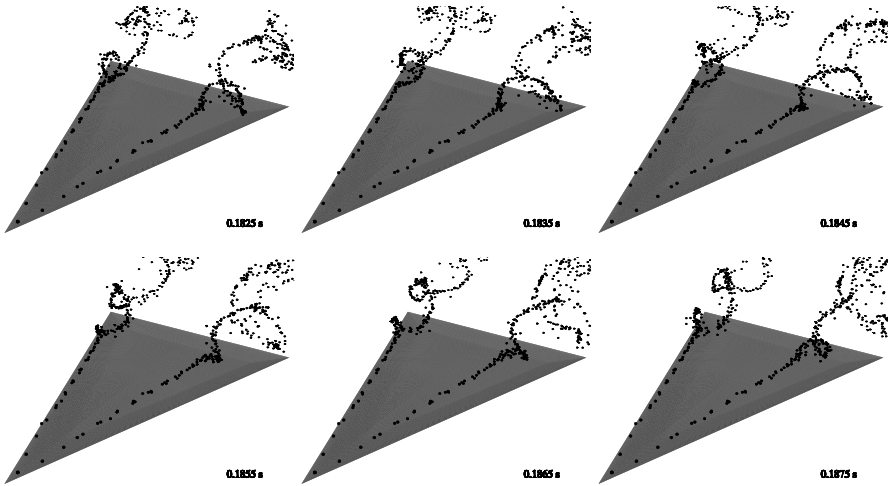


Figure 28: Snap shots of time-dependent particles at different instances in time ( $M_\infty = 0.2$ ,  $\alpha = 30^\circ$ , Euler)

Figure 28 shows snap shots of some time-dependent particles from the full-span Euler simulation at different instances in time. Note that time increases from left to right, top to bottom. Particles were released at fifteen seed locations along a line coinciding with the vortex axis upstream of the point of vortex breakdown. Their pathlines were traced and animated. The particles form a streakline that varies with time. The particles follow the straight vortex core axis up to the point of vortex breakdown, where they abruptly decelerate and start to spiral on helical path around an imaginary extension of the upstream vortex axis, indicating spiral-type vortex breakdown. It can be observed that the sense of the spiral windings is opposite to the direction of rotation of the upstream vortex, however, the rotation of the windings is in the same direction as the rotation of the upstream vortex, compare Fig. 8.

Vortex cores were also extracted independently from the solution files using the feature extraction tool of the commercial visualization program EnSight and played back sequentially to produce an animation. This and other flow-field visualization videos are found on the accompanying CD-ROM.

The above results demonstrate that the flow field is inherently unsteady. A *time-accurate* simulation of a *full-span* model is necessary to capture all aspects of the flow field at high angle of attack.

## Paper D

Paper D is a continuation of the work presented in Paper C. It extends the physical modeling of the flow over the  $70^\circ$  full-span delta wing to *viscous* unsteady flow. Detached-Eddy Simulations (DES) were done on a Navier-Stokes grid for one angle

of attack using implicit dual time stepping. A time step study was conducted on a semi-span delta-wing model to verify time-accuracy. The results were compared to the experimental data by Mitchell [24, 39]. Grid refinement improved the comparison with the experimental data. Fig. 29 compares the longitudinal velocity component  $u/U_\infty$  in cross-planes at four distances along the root chord for time-averaged DES on a refined grid (left) and the experiment (right).

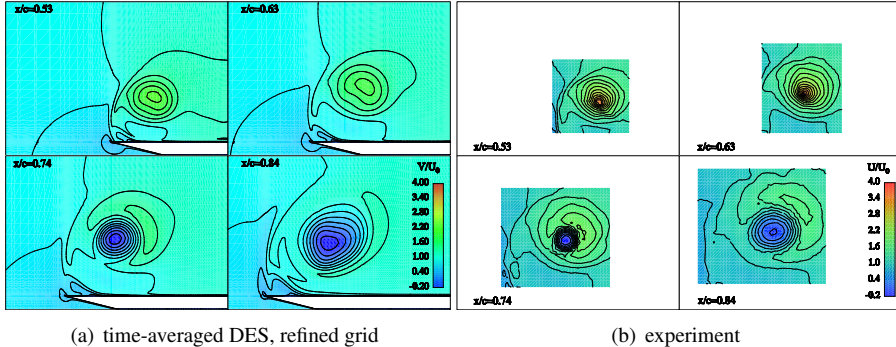


Figure 29: Computed (left) and measured (right) longitudinal velocity component in vertical planes at four different chordwise stations ( $M_\infty = 0.2$ ,  $Re = 1.56 \times 10^6$ ,  $\alpha = 27^\circ$ )

The geometry of the vortex is seen to be in good agreement with the experiment. Also the overall velocity field is well predicted by DES. However, the numerical simulation underestimated the maximum velocities in the core of the vortex upstream of vortex breakdown. An even finer grid would be needed to better resolve this critical region of the flow. These first results also showed that DES is capable of predicated the fluctuating vortex breakdown location quite accurately. The surface pressure distribution, however, was underestimated. An inter-code comparison revealed that this was true for all AVT-080 participants. Actually, inter-code comparison of the computed surface  $C_p$  between the members of AVT-080 was excellent [163]. Later, this could be traced back to excessive blockage effects in the experiment (blockage was 6%). The wind-tunnel measurements were repeated at ONERA, however, at a nominally lower angle of attack ( $\alpha = 26^\circ$  instead of  $\alpha = 27^\circ$ ), resulting in perfect agreement between the measured and computed surface pressure distributions [164].

## Paper E

Acknowledging the shortcomings of wind-tunnel measurements of the flow over delta wings, I turned my attention to experimental flight-test results and more realistic delta-wing configurations. Flight data for CFD code validation has been obtained on the surface of the NASA F-16XL-1 aircraft at subsonic and transonic speeds as documented by Lamar [165]. This data is unique both in that it is for a high-performance delta-wing aircraft and it is publicly accessible on the internet [166]. Furthermore, the data is not subject to wind tunnel blockage-, scaling- or Reynolds number effects.

After learning of this high Reynolds number flight-test data set, I joined with other European and American participants in one ‘facet’ of the NATO Research and Technology Organization (RTO) Applied Vehicle Technology (AVT) task group AVT-113 “Understanding and Modelling Vortical Flows to Improve the Technology Readiness Level for Military Aircraft.” This facet is named the “Cranked Arrow Wing Aerodynamics Project International” (CAWAPI). The aim is to develop and document the best practices for each CFD code so as to raise its technology readiness level when applied to this class of aircraft. The existing experimental flight-test results are used for comparison and for improving the understanding of vortical flows.

In order for these comparison to be made and reported, several steps had to be taken, such as finalizing a complete numerical surface description of the aircraft geometry (including missiles and air-dams), generation of structured and unstructured grid files and opening of a ‘virtual laboratory’ for exchanging experimental and CFD data. These steps were performed as a shared effort.

An initial set of CFD solutions has been computed using different novel turbulence models and has been compared to the experimental data. This is reported in Paper E. The computed mean-flow solutions were used to generate an adaptively refined grid by cell subdivision based on a novel sensor for identifying vortices. The newly generated tetrahedral elements are shown in Fig. 30. The grid is seen to have been refined in the vortical flow region, capturing the primary wing vortex, parts of the secondary wing vortex, the vortex originating at the air dam and a vortex over the outer part of the wing close to the wing tip.



Figure 30: New tetrahedral cells generated by adaptive grid refinement (vortex sensor); F-16XL grid

## Paper F

This paper deals with the interactive exploration of the unsteady flows presented in the previous papers in a virtual-reality environment. This novel postprocessing technique offers interactivity, 3D visualization and immersion compared to pre-computed plots, pre-computed animations and 2D visualization in traditional postprocessing.

The highly interactive three-dimensional nature of virtual reality provides an intuitive exploration environment for the analysis of the complex three-dimensional structures arising in the time-dependent delta-wing simulations presented above. A variety of standard visualization techniques are supported in the “virtual windtunnel”. However, the intuitive interaction techniques facilitate the selection of different representations of the pre-computed data (e.g. repositioning of cutting planes). This is illustrated in Fig. 31, which shows the interactive visualization of the unsteady flow over the delta wing described in Paper C in the virtual-reality environment at KTH. The delta wing and an instant in time of the corresponding unsteady flow field are projected mainly on the rear wall of the six-sided virtual-reality system. The flow field is visualized using a cutting plane colored by pressure coefficient, pathlines colored by velocity magnitude and animated particles colored by velocity magnitude. Both the cutting plane and the pathlines are controlled interactively. Apart from presenting other CFD applications, the paper also discusses the advantages and disadvantages of the virtual-reality system at KTH.

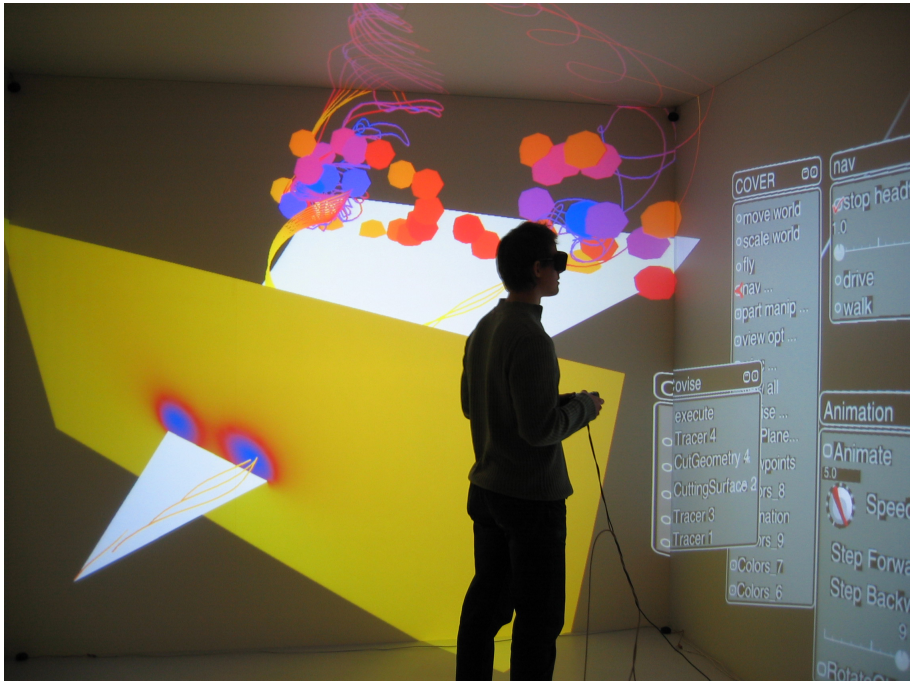


Figure 31: Time-dependant flow over delta wing visualized in virtual-reality environment (stereo mode switched off)

## Paper G

The time-dependent computations described in Papers C through E proved to be very CPU-intensive, mainly because the inner loop of the dual time-stepping scheme in both NSMB and Edge is computationally too expensive. This motivated work on algorithmic efficiency, which is described in Paper G. The most promising candidate turned out to be the Recursive Projection Method (RPM), an implicit-explicit algorithm, which was extended from a method for bifurcation analysis to a convergence accelerator for dual time stepping. The algorithm and its implementation into the flow solver Edge was verified against the native Edge iteration scheme by driving the residual of the steady state simulation of the laminar flow around a circular cylinder at  $Re = 100$  to machine accuracy. Following the verification of the scheme, it was used to accelerate unsteady simulations of the periodic self-excited viscous flow around a circular cylinder at  $Re = 100$ , demonstrating worth-while CPU-time savings of about 50%. This is illustrated in Fig. 32, which shows the number of inner iterations (function evaluations) as a function of the number of outer time (steps) using the native Edge iteration scheme and RPM. The numerical experiments also supported that it is slightly favorable to reuse and update information that RPM extracted at previous outer time steps (restart/update approach).

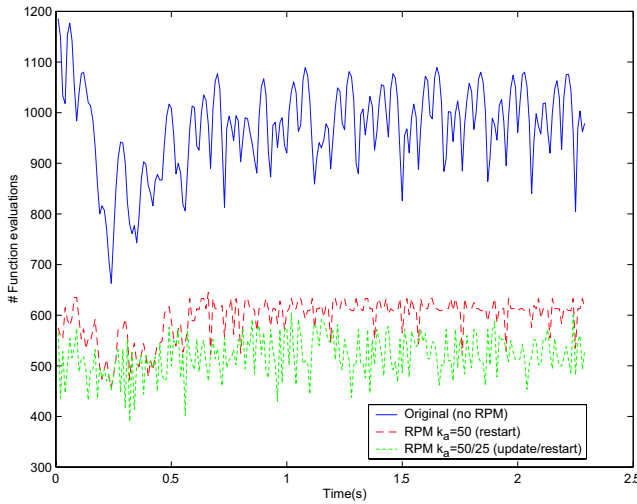


Figure 32: Comparison between the native Edge iteration scheme and RPM; periodic self-excited viscous flow around a circular cylinder at  $Re = 100$

## Paper H

The last paper described the extension of the RPM implementation to one- and two-equation turbulence models. The modified code was used to compute the unsteady turbulent buffet flow around an 18%-thick biconvex airfoil at transonic speed. On average, the inner loop of the modified code converged two times faster to a predefined

convergence criterion than the original code (restart approach). An average acceleration by a factor of 2.5 could be achieved by reusing and updating information that RPM extracted at previous outer time steps (restart/update approach). This is illustrated in Fig. 33, where the blue solid line represents the number of inner iterations versus the number of outer time steps without RPM and the red dashed and green dot-dashed lines denote the total number of function evaluations with the restart approach and the combined restart/update approach, respectively. The additional computational cost that RPM incurs was shown to be negligible. In summary, for unsteady turbulent computations, the overall efficiency of the code was more than doubled by using RPM.

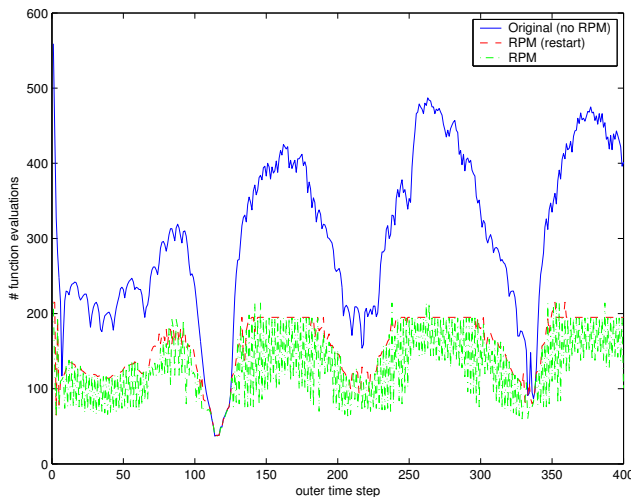


Figure 33: Comparison between restart and restart/update approach for turbulent RPM computations of the unsteady turbulent buffet flow around an 18%-thick biconvex airfoil at transonic speed

## Conclusions

The results presented in the present thesis expand the general knowledge of the vortical flow over delta wing configurations at high angle of attack and point out the numerical parameters that have been found to influence the numerical results. Major achievements and most important findings of the thesis are:

- Vortex breakdown over delta wings is practically an inviscid phenomenon. The Euler and Navier-Stokes equations predict the same breakdown location when the same numerical grid is used.
- The nonlinear interaction between a forebody vortex and a burst wing leading-edge vortex can be predicted using the Navier-Stokes equations and a suitable numerical grid.
- Computations of vortical flows, especially vortex breakdown, are highly sensitive to local grid resolution and grid topology.
- Vortical flows at high incidence are inherently unsteady and require time-accurate computations, especially for predicting the breakdown location and capturing asymmetry in the flow.
- Time-accurate Euler simulations of a full-span delta wing appeared to capture vortex interactions. The simulations were able to capture the helical mode instability (spiral-type breakdown) as well as fluctuations of breakdown location. Intermittent bubble-type breakdown was also observed and found responsible for asymmetry in the port and starboard breakdown location.
- Detached-Eddy Simulations (DES) were shown to be promising for time-accurate viscous computations of separated flows in general and vortex breakdown in particular. The computational cost of the simulation of a given physical time interval is very high, however.
- The lessons learned for generic wind-tunnel scale models throughout the course of the thesis have been applied to the steady and unsteady simulation of a realistic delta-wing aircraft configuration, the F-16XL, for which extensive flight-test and wind-tunnel data is available. This simulation allowed comparison between numerical and experimental data at flight Reynolds numbers as opposed to wind-tunnel Reynolds numbers, circumventing the problem of modeling transition. The higher geometrical complexity was seen to leads to higher physical complexity.
- The analysis of unsteady flow simulations of delta-wing configurations was shown to be facilitated by a virtual-reality environment. The immersive environment improved the understanding of the spatial and temporal evolution of three-dimensional structures in the flow field, such as spiral and bubble-type breakdown, etc.

- Advances were made in improving the algorithmic efficiency of dual time stepping by considering the Recursive Projection Method for time-dependent CFD simulations.

## Acknowledgements

I wish to express my sincere gratitude to my research advisor, Prof. Arthur Rizzi, for his guidance spanning my undergraduate and graduate education and for giving me the opportunity to attend many interesting and stimulating conferences, symposiums and seminars.

I would like to thank all my colleagues at the Department of Aeronautical and Vehicle Engineering at KTH for a stimulating and pleasant working environment. A sincere thanks to Yann Le Moigne for the close collaboration and for many helpful discussions.

Jan B. Vos, CFS Enginnering SA, Lausanne, Switzerland, has to be thanked for sharing his expert knowledge of the structured flow solver NSMB and for always taking time to answer my questions. Numerous helpful conversations with the researchers and engineers at EADS/Airbus and CERFACS, Toulouse, France, are also gratefully acknowledged.

I am also indebted to Bengt Winzell, Swedish Defence Research Agency (FOI), who made it possible for me to work at FOI on the unstructured CFD code Edge. I greatly appreciate the many stimulating discussions I had with the researchers at FOI, especially with Peter Eliasson and Jonathan Smith.

The cooperation with Joakim Möller, NADA, KTH, on RPM has been very exciting and challenging, and is gratefully acknowledged. This work was very much inspired by Jesper Oppelstrup, NADA, who guided our work with enthusiasm and competence.

I felt especially honored to join the NATO Advanced Vehicle Technology (AVT) task groups “Vortex Breakdown over Slender Wings” (AVT-080) and “Understanding and Modelling Vortical Flows to Improve the Technology Readiness Level for Military Aircraft” (AVT-113). This enabled me to meet some of the most eminent authorities in my field of research. Special thanks to John E. Lamar, NASA Langley, for his interest and encouragement.

PDC, the Parallel Computing Center at KTH, and NSC, the Swedish National Supercomputing Center at Linköping University, provided the computer resources to run the numerical calculations.

On a personal note, I would like to thank my family, especially my parents, for their constant support, encouragement, inspiration, understanding and endless love, despite the distance: Danke !

To Eun-Kyung I just want to say: 너를 아주 매우 사랑하십시요 !

Stockholm, February 2005.

*Stefan Görtz*



## References

- [1] Rom, J., *High Angle of Attack Aerodynamics*, Springer Verlag, New York, 1992.
- [2] Rizzi, A. and Engquist, B., "Selected Topics in the Theory and Practice of Computational Fluid Dynamics," *Journal of Computational Physics*, Vol. 72, No. 1, September 1987.
- [3] Raj, P., "Aircraft Design in the 21st Century: Implications for Design Methods," *AIAA Paper 98-2895*, 1998.
- [4] Lamar, J. E., "Understanding and Modeling Vortical Flows to Improve the Technology Readiness Level for Military Aircraft," Terms of Reference, NATO RTO Advanced Vehicle Technology Panel AVT-E-10/RTG, July 2002.
- [5] Lovell, D. A., "Military Vortices," *NATO RTO Symposium on Advanced Flow Management, Part A - Vortex Flow and High Angle of Attack*, 2001, Loen, Norway, RTO MP-069(I)-(SYA)-KN1.
- [6] Arthur, M., "Vortical Flows over Military Air Vehicles," *QNET-CFD Network Newsletter*, Vol. 1, No. 2, July 2001, pp. 32–34.
- [7] Wentz, W. H., "Vortex-Fin Interaction on a Fighter Aircraft," *AIAA Paper 87-2474*, 1987.
- [8] Dhah, G. H., Grafton, S. B., Guynn, M. D., Branson, J. M., Dansberry, B. E., and Patel, S. R., "Effect of Vortex Flow Characteristics on Tail Buffet and High Angle-of-Attack Aerodynamics of a Twin-Tail Fighter Configuration," *Proceedings of the High-Angle-of-Attack Technology Conference, NASA LARC, Hampton, VA*, November 1990.
- [9] Beyers, M. and Eriksson, L.-E., "Why is LEX Vortex Breakdown on the F/A-18 Configuration Insensitive to Reynolds Number?" *AIAA Paper 2001-0690*, 2001.
- [10] Fisher, D. F., Del Frate, J., and Richwine, D. M., "In-Flight Flow Visualization Characteristics of the NASA F-18 High Alpha Research Vehicle at High Angles of Attack," NASA Technical Memorandum 4193, May 1990.
- [11] Raj, P., Finley, D. B., and Ghaffari, F., "An Assessment of CFD Effectiveness for Vortex-Flow Simulation to Meet Preliminary Design Needs," *NATO RTO Symposium on Advanced Flow Management*, 2001, Loen, Norway, RTO MP-069(I)-(SYA)-47.
- [12] Hoeijmakers, H. W. M., "Modeling and Numerical Simulation of Vortex Flow in Aerodynamics," AGARD CP-494, Vortex Flow Aerodynamics, July 1991.
- [13] Hoang, N., Rediniotis, O. K., and Telionis, D. P., "3-D LDV Measurements over a Delta Wing in Pitch-Up Motion," *AIAA Paper 93-0185*, 1993.
- [14] Spalart, P. R. and Bogue, D. R., "The role of CFD in aerodynamics, off-design," *Aeronautical Journal*, June 2003, pp. 322–329.
- [15] Lamar, J. E., "Understanding and Modeling Vortical Flows to Improve the Technology Readiness Level for Military Aircraft," Technical Activity Proposal, NATO RTO Advanced Vehicle Technology Panel AVT-E-10/RTG, July 2002.
- [16] Cummings, R. M., Forsythe, J. R., Morton, S. A., and Squires, K. D., "Computational challenges in high angle of attack flow prediction," *Progress in Aerospace Sciences*, Vol. 39, 2003, pp. 369–384.
- [17] Le Moigne, Y., *CFD Simulations of a Delta Wing Pitching to High Alpha*, Licentiate thesis, Royal Institute of Technology (KTH), Department of Aeronautics, Stockholm, Sweden, February 2002, Skrift 2002-7.
- [18] Anderson, J. D., *Fundamentals of Aerodynamics*, McGraw-Hill, 2nd ed., 1991.
- [19] Campbell, J. F. and Chambers, J. R., *Patterns in the Sky - Natural Visualization of Aircraft Flow Fields*, NASA Langley Research Center, NASA SP-514, 1994.
- [20] Payne, F. M., Ng, T. T., Nelson, R. C., and Schiff, L. B., "Visualization and Flow Surveys of the Leading-Edge Vortex Structure on Delta Wing Planforms," *AIAA Paper 86-0330*, 1986.
- [21] Payne, F. M., *The Structure of Leading Edge Vortex Flows Including Vortex Breakdown*, Ph.D. thesis, Univ. of Notre Dame, Dept. of Aerospace and Mechanical Engineering, Notre Dame, IN, 1987.
- [22] Lowson, M. V., "The Three Dimensional Vortex Sheet Structure on Delta Wings," AGARD CP-438, Fluid Dynamics of Three-Dimensional Turbulent Shear Flows and Transition, 1988.

- [23] Riley, A. J. and Lawson, M. V., "Development of a Three-Dimensional Free Shear Layer," *Journal of Fluid Mechanics*, Vol. 369, 1998, pp. 49–89.
- [24] Mitchell, A. M., *Caractérisation et contrôle de l'éclatement tourbillonnaire sur une aile delta aux hautes incidences*, Ph.D. thesis, Université Paris VI, Paris, France, July 2000.
- [25] Polhamus, E. C., "Predictions of Vortex-Lift Characteristics by a Leading-Edge Suction Analogy," *Journal of Aircraft*, Vol. 8, No. 4, April 1971, pp. 193–199.
- [26] Hummel, D., "On the Vortex Formation over a Slender Wing at Large Incidence," AGARD CP-247, High Angle of Attack Aerodynamics, 1978.
- [27] Wentz, W. H. and Kohlman, D. L., "Vortex Breakdown on Slender Sharp-Edged Wings," *Journal of Aircraft*, Vol. 8, 1971, pp. 156–161.
- [28] Délery, J. M., "Aspects of Vortex Breakdown," *Progress in Aerospace Sciences*, Vol. 30, 1994, pp. 1–59.
- [29] Nelson, R. C. and Pelletier, A., "The unsteady aerodynamics of delta wings and aircraft undergoing large amplitude maneuvers," *Progress in Aerospace Sciences*, Vol. 39, 2003.
- [30] Gursul, I., "Review of unsteady vortex flows over delta wings," *AIAA Paper 2003-3942*, 2003.
- [31] Gursul, I., "Review of Unsteady Vortex Flows over Slender Delta Wings," *Journal of Aircraft*, in print.
- [32] Werlé, H., "Quelques résultats expérimentaux sur les ailes en flèches, aux faibles vitesses, obtenus en tunnel hydrodynamique," *La Recherche Aéronautique* 41, 1954.
- [33] Peckham, D. H. and Atkinson, S. A., "Preliminary Results of Low Speed Wind Tunnel Tests on a Gothic Wing of Aspect Ratio 1.0," Report CP-508, Aeronautical Research Council, 1957.
- [34] Elle, B. J., "An investigation at low speed of the flow near the apex of thin delta wings with sharp leading edges," Reports and Memoranda 3176, Aeronautical Research Council, January 1958.
- [35] Lambourne, N. C. and Bryer, D. W., "The Bursting of Leading-Edge Vortices - Some Observations and Discussions of the Phenomenon," Reports and Memoranda 3282, Aeronautical Research Council, 1962.
- [36] Kegelman, J. and Roos, F., "Effects of Leading-Edge Shape and Vortex Burst on the Flowfield of a 70 Degree Sweep Delta-Wing," *AIAA Paper 89-0086*, 1989.
- [37] Kegelman, J. and Roos, F., "The Flowfield of Bursting Vortices over Moderately Swept Delta Wings," *AIAA Paper 90-0599*, 1990.
- [38] Payne, F. M., Ng, T. T., and Nelson, R. C., "Visualisation and Flow Surveys of the Leading Edge Vortex Structure on Delta Wing Planforms," *AIAA Paper 86-0303*, 1986.
- [39] Mitchell, A. M., Barberis, D., and Délery, J., "Oscillation of Vortex Breakdown Location and Its control by Tangential Blowing," *AIAA Paper 98-2914*, 1998.
- [40] Payne, F. M., Ng, T. T., and Nelson, R. C., "Experimental Study of the Velocity Field on a Delta Wing," *AIAA Paper 87-1231*, June 1987.
- [41] Greenwell, D. I., "Pitfalls in the Interpretation of Delta Wing Flow Visualization," *NATO RTO Symposium on Advanced Flow Management*, 2001, Loen, Norway, RTO MP-069(I)-(SYA)-05.
- [42] Huang, X. Z. and Hanff, E. S., "Flow Physics of Leading-Edge Vortex-Breakdown," *AIAA Paper 98-31536*, 1998.
- [43] Wentz, W. H. and Kohlman, D. L., "Vortex Breakdown on Slender Sharp-Edged Wings," *AIAA Paper 69-778*, 1969.
- [44] Lawson, M. V. and Riley, A. J., "Vortex Breakdown Control by Delta Wing Geometry," *AIAA Paper 94-3487*, 1994.
- [45] Hemsch, M. J. and Luckring, J. M., "Connection between Leading-Edge Sweep, Vortex Lift, and Vortex Strength for Delta Wings," *Journal of Aircraft*, Vol. 27, 1990, pp. 473–475.
- [46] Miau, J. J., Kuo, K. T., Liu, W. H., Hsieh, S. J., and Chou, J. H., "Flow Developments Above 50-Deg Sweep Delta Wings with Different Leading-Edge Profiles," *Journal of Aircraft*, Vol. 32, No. 4, 1995, pp. 787–794.

- [47] O'Neil, P., Roos, F., Kegelman, J., Barnett, R., and Hawk, J., "Investigation of Flow Characteristics of a Developed Vortex," Final Report NADC-89114-60, McDonnell Aircraft Company, May 1989.
- [48] Agrawal, S., Robinson, B. A., and Barnett, R. M., *Prediction of Vortex Breakdown on a Delta Wing*, The Fifth Symposium on Numerical and Physical Aspects of Aerodynamic Flows, California State University, 1993.
- [49] Erickson, G. E., "Water-Tunnel Studies of Leading-Edge Vortices," *Journal of Aircraft*, Vol. 19, No. 6, 1982, pp. 442–448.
- [50] Lowson, M. V., "Some Experiments with Vortex Breakdown," *Journal of the Royal Aeronautical Society*, Vol. 68, May 1964, pp. 343–346.
- [51] Soltani, M. R. and Bragg, M. B., "Measurements on an Oscillating 70-Deg Delta Wing in Subsonic Flow," *Journal of Aircraft*, Vol. 27, No. 3, 1990, pp. 211–217.
- [52] Kjelgaard, S. D., Sellers, W. L., and Watson, R. P., "The Flowfield over a 75 Degree Swept Delta Wing at 20.5 Degrees Angle of Attack," *AIAA Paper 86-1775*, 1986.
- [53] Wolffelt, K. W., "Investigation of the Movements of Vortex Burst Position with Dynamically Changing Angle of Attack for a Schematic Delta Wing in a Water Tunnel With Correlation to Similar Studies in a Wind Tunnel," AGARD CP-4123, 1986.
- [54] Hummel, D., "Untersuchungen über das Aufplatzten der Wirbel an schlanken Deltaflügeln," *Zeitung für Flugwissenschaften*, Vol. 13, No. 5, 1965.
- [55] Earnshaw, P. B. and Lawford, J. A., "Low Speed Wind Tunnel Experiments on a Series of Sharp-edged Delta Wings," R & M 3424, Aeronautical Research Council, August 1964.
- [56] Gursul, I., "Unsteady Flow Phenomena over Delta Wings at High Angle of Attack," *AIAA Journal*, Vol. 32, No. 2, February 1994, pp. 225–231.
- [57] Eriksson, L.-E. and Rizzi, A., "Computations of Vortex Flow around Wings using the Euler Equations," *Notes on Numerical Fluid Mechanics*, Vol. 5, 1982, pp. 87–105.
- [58] Murman, E. M. and Rizzi, A., "Application of Euler Equations to Sharp Edge Delta Wings With Leading Edge Vortices," AGARD CP-412, Computational Fluid Dynamics in Aeronautics, November 1986.
- [59] Rizzi, A. and Eriksson, L. E., "Computation of the flow around wings based on the Euler equations," *Journal of Fluid Mechanics*, Vol. 148, 1984, pp. 45–71.
- [60] Rizzi, A., Eriksson, L.-E., Schmidt, W., and Hitzel, S., "Numerical Solutions of the Euler Equations Simulating Vortex Flows around Wings," AGARD CP-342, Aerodynamics of Vortical Type Flows in Three Dimensions, 1983.
- [61] Rizzi, A. and Purcell, C. J., "On the computation of transonic leading-edge vortices using the Euler equations," *Journal of Fluid Mechanics*, Vol. 181, 1987, pp. 163–195.
- [62] Rizzi, A. and Eriksson, L.-E., "Computation of inviscid incompressible flow with rotation," *Journal of Fluid Mechanics*, Vol. 153, 1985, pp. 275–312.
- [63] Sirbaugh, J. R., "Euler Analysis of the AFWAL 65° Delta Wing," *AIAA Paper 87-2272*, 1987.
- [64] Scherr, S. and Das, A., "Basic Analysis of the Flow Fields of Slender Delta Wings Using the Euler Equations," ICAS Paper 88-5.9.2, Proceeding of the 16<sup>th</sup> Congress of ICAS, 1988.
- [65] Rizzi, A., "Three-Dimensional Solutions to the Euler Equations with One Million Grid Points," *AIAA Journal*, Vol. 23, No. 12, December 1985, pp. 1986–1987.
- [66] Rizzi, A., Müller, B., and Purcell, C. J., "Comparison of Euler and Navier-Stokes Solutions for Vortex Flow over a Delta Wing," *AIAA Paper 87-2347*, 1987.
- [67] Rizzi, A. and Mü, B., "Comparison of Euler and Navier-Stokes solutions for vortex flow over a delta wing," *The Aeronautical Journal of the Royal Aeronautical Society*, April 1988.
- [68] Raj, P., Sikora, J. S., and Keen, J. M., "Free-Vortex Flow Simulation using a Three-Dimensional Euler Aerodynamic Method," *Journal of Aircraft*, Vol. 25, No. 2, 1988, pp. 128–134.
- [69] Hartwich, P. M., Hsu, C. H., Luckring, J. M., and Liu, C. H., "Numerical Study of the Vortex Burst Phenomenon for Delta Wings," *AIAA Paper 88-0505*, 1988.

- [70] Ekaterinaris, J. A. and Schiff, L. B., "Vortical Flows over Delta Wings and Numerical Prediction of Vortex Breakdown," *AIAA Paper 90-0102*, 1990.
- [71] Ekaterinaris, J. A. and Schiff, L. B., "Numerical Simulation of the Effects of Variation of Angle of Attack and Sweep Angle on Vortex Breakdown over Delta Wings," *AIAA Paper 90-3000CP*, 1990, pp. 59–67.
- [72] Fujii, K. and Schiff, L. B., "Numerical Simulations of Vortical Flows over a Strake-Delta Wing," *AIAA Journal*, Vol. 27, No. 9, 1989, pp. 1153–1162.
- [73] Arthur, M. T., Kordulla, W., Brandsma, F. J., and Ceresola, N., "Grid Adaption in Vortical Flow Simulations," *AIAA Paper 97-2308*, 1997.
- [74] Borsi, M., Kordulla, W., Hoeijmakers, H. W. M., and Williams, B. R., "Comparison of solution of various Navier-Stokes solvers and one Euler solver for the flow about a sharp edged cropped delta wing (under the auspices of IEPG-TA15)," *Proceedings of 1993 European Forum: Recent Developments and Applications in Aeronautical CFD*, 1993, pp. 5.1–5.11, RAeS conference, Bristol, England.
- [75] Pirzadeh, S. Z., "Vortical Flow Prediction using an Adaptive Unstructured Grid Method," *NATO RTO Symposium on Advanced Flow Management, Part A - Vortex Flow and High Angle of Attack*, 2001, Loen, Norway, RTO MP-069(I)-(SYA)-13.
- [76] Gordnier, R. E., "Numerical Simulation of a 65-Degree Delta Wing Flowfield," *Journal of Aircraft*, Vol. 34, No. 4, July-August 1997, pp. 492–499.
- [77] Visbal, M. R., "Computed Unsteady Structure of Spiral Vortex Breakdown on Delta Wings," *AIAA Paper 96-2074*, 1996.
- [78] Visbal, M. R. and Gaitonde, D. V., "High-Order-Accurate Methods for Complex Unsteady Subsonic Flows," *AIAA Journal*, Vol. 37, No. 10, 1999, pp. 1231–1239.
- [79] Müller, J. and Hummel, D., *An analysis of vortex breakdown predicted by a time-accurate Euler code*, Notes on Numerical Fluid Mechanics, Vieweg Verlag, Braunschweig, 1999, pp. 331–338.
- [80] Müller, J. and Hummel, D., "Numerical Analysis of the Unsteady Flow above a Slender Delta Wing at Large Angles of Attack," *ICAS Paper 2000-252*, 2000.
- [81] Morton, S., Forsythe, J., Mitchell, A., and Hajek, D., "DES and RANS Simulations of Delta Wing Vortical Flows," *AIAA Paper 2002-0587*, 2002.
- [82] Morton, S. A., Forsythe, J. R., Squires, K. D., and Wurtzler, K. E., "Assessment of Unstructured Grids for Detached-Eddy Simulation of High Reynolds Number Separated Flows," *Proceedings of the 8<sup>th</sup> International Conference on Grid Generation in Computational Field Simulations*, June 2002.
- [83] Mitchell, A., Morton, S. A., and Forsythe, J. R., "Analysis of Delta Wing Vortical Substructures using Detached-Eddy Simulation," *AIAA Paper 2002-2968*, 2002.
- [84] Estorf, M. and Hummel, D., *Validation and Verification of CFD and Analytical Solutions for the Vortical Flow over Slender Delta Wings at High Incidence*, chap. Euler and Navier-Stokes Simulations for Vortex Breakdown on a Delta Wing, RTO TR-084, NATO, 2005.
- [85] Vos, J. B., Leyland, P., van Kemenade, V., Gacherieu, C., Duquesne, N., Lötstedt, P., Weber, C., Ytterström, A., and Saint Requier, C., *NSMB Handbook 4.5*, March 2000.
- [86] Vos, J. B., Bohbot, J., Champagneux, S., Cormier, J., Darraq, D., Kozuch, L., Souleres, T., Duquesne, N., Ytterström, A., Saint Requier, C., Le Moigne, Y., Gacherieu, C., Persson, I., and Sillen, M., *NSMB 5.5 User Guide*, June 2002.
- [87] Vos, J. B., Rizzi, A., Corjon, A., Chaput, E., and Soinne, E., "Recent Advances in Aerodynamics inside the NSMB (Navier-Stokes Multi Block) Consortium," *AIAA Paper 98-0225*, 1998.
- [88] Gacherieu, C., Weber, C., and Coriolis, G., "Assessment of Algebraic and One-Equation Turbulence Models for the Transonic Turbulent Flow around a Full Aircraft Configuration," *AIAA Paper 98-2737*, 1998.
- [89] Weber, C. et al., "Recent Applications in Aerodynamics with NSMB Structured MultiBlock Solver," *Frontiers of Computational Fluid Dynamics*, World Scientific Publishing 1998.

- [90] Darracq, D., Champagneux, S., and Corjon, A., "Computation of Unsteady Turbulent Airfoil Flows with an Aeroelastic AUSM+ Implicit Solver," *AIAA Paper 98-2411*, 1998.
- [91] Yee, H. C., *A Class of High-Resolution Explicit and Implicit Shock-Capturing Methods*, VKI LS 1989-4, Computational Fluid Dynamics, 1989.
- [92] Jameson, A., Schmidt, W., and Turkel, E., "Numerical Solutions of the Euler Equations by Finite Volume Methods using Runge-Kutta Time Stepping," *AIAA Paper 81-1259*, 1981.
- [93] Jameson, A. and Turkel, E., "Implicit Schemes and LU Decompositions," *Mathematics of Computation*, Vol. 37, No. 156, October 1981.
- [94] Weber, C., *Développement de méthode implicite pour les équations de Navier-Stokes moyennées et la simulation des grandes échelles: Application à l'aérodynamique externe*, Ph.D. thesis, Centre Européen de Recherche et de Formation Avancée en Calcul Scientifique (CERFACS), Toulouse, France, 1998.
- [95] Turkel, E., Vatsa, V. N., and Radespiel, R., "Preconditioning Methods for Low-Speed Flows," CR 201605, NASA, October 1996.
- [96] Petterson, K., *The Aerodynamics of Slender Aircraft Forebodies at High Angle of Attack*, Ph.D. thesis, Cranfield University, College of Aeronautics, April 2001.
- [97] Champagneux, S., "Vers le Couplage Fluide-Structure – Méthode ALE pour l'Aérodynamique Instationnaire," Tech. rep., DEA de Mécanique des Fluides de Toulouse, Institut National Polytechnique de Toulouse, 1997.
- [98] Bohbot, J., Bertin, D., and Darraq, D., "A Conservative Patched Grid Algorithm for Turbulent Flow Computations of 3D Complex Aircraft Configurations," *European Congress on Computational Methods in Applied Sciences and Engineering, ECCOMAS 2000*, 2000.
- [99] Jameson, A., "Solution of the Euler equations for two-dimensional transonic flow by a multigrid method," *Applied Math. Comput.*, Vol. 13, 1983, pp. 327–355.
- [100] Merazzi, S., *MEM-COM: An Integrated Memory and Data Management System - MEM-COM Reference Manual Version 6.2*, SMR Corporation, Bienna, Switzerland, November 1994.
- [101] Sjögren, T. and Eliasson, P., "Description and Validation of EDGE," FFA TN 1998-61, The Aeronautical Research Institute of Sweden (FFA), 1998.
- [102] Eliasson, P., "EDGE - A Navier-Stokes Solver for Unstructured Grids," Tech. Rep. FOI-R-0298-SE, Swedish Defence Research Agency (FOI), Division of Aeronautics (FFA), Stockholm, Sweden, December 2001.
- [103] Eliasson, P., "EDGE, a Navier-Stokes solver for unstructured grids," *Proc. To Finite Volumes for Complex Applications III*, 2002, pp. 527–534.
- [104] Swedish Defence Research Agency (FOI), Aeronautics Div. (FFA), "Edge 3.2 Installation and User Guide," <http://www.edge.foi.se>, October 2004, accessed 12/2004.
- [105] Spalart, P. R. and Allmaras, S. R., "A One-Equation Turbulence Model for Aerodynamic Flows," *AIAA Paper 92-0439*, 1992.
- [106] Wilcox, D. C., "Reassessment of the Scale Determining Equation for Advances Turbulence Models," *AIAA Journal*, Vol. 6, No. 11, 1988.
- [107] Wallin, S. and Johansson, A., "A Complete Explicit Algebraic Reynolds Stress Model for Incompressible and Compressible Turbulent Flows," *Journal of Fluid Mechanics*, Vol. 403, 2000, pp. 89–132.
- [108] Jameson, A., "Time dependent calculations using multigrid, with application to unsteady flows past airfoils and wings," *AIAA Paper 91-1596*, 1991.
- [109] Tysell, L., "An Advancing Front Grid Generation System for 3D Unstructured Grids," *ICAS-94-2.5.1*, 1994.
- [110] Tysell, L., "Grid Deformation on Hybrid Grids," *8th International Conference on Numerical Grid Generation in Computational Field Simulations*, 2002.
- [111] Wallin, S., "Standardized Data Format," FFAP A-950, The Aeronautical Research Institute of Sweden (FFA), October 1992.

- [112] Schroff, G. M. and Keller, B., “Stabilization of Unstable Procedures: The Recursive Projection Method,” *SIAM J. Numer. Anal.*, Vol. 30, No. 4, August 1993, pp. 1099–1120.
- [113] Rizzi, A. and Eriksson, L.-E., “Unigrid projection method to solve the Euler equations for steady state transonic flow,” *8th Intern. Conf. on Numerical Methods in Fluid Dynamics*, Lecture Notes in Physics, Springer Verlag, 1982.
- [114] Jarausch, H., “Analyzing stationary and periodic solutions of systems of parabolic partial differential equations by using singular subspaces as reduced basis,” Tech. rep., Inst. f. Geometrie u. Prakt. Mathematik, Achen, Germany, 1993.
- [115] Jarausch, H. and Mackens, W., *Numerical methods for bifurcation problems*, Vol. 70, chap. Numerical treatment of bifurcation branches by adaptive condensation, Birkhäuser, Basel, 1984, pp. 269–309.
- [116] Jarausch, H. and Mackens, W., *Progress in Scientific Computing 7*, chap. Computing bifurcation diagrams for large non-linear variational problems, Birkhäuser, Basel, 1987.
- [117] Davidson, B. D., “Large-Scale Continuation and numerical Bifurcation for Partial Differential Equation,” *SIAM J. Numer. Anal.*, Vol. 34, 1997, pp. 2008–2027.
- [118] Lust, K., *Numerical bifurcation analysis of periodic solutions of partial differential equations*, Ph.D. thesis, Katholieke Universiteit, Leuven, 1997.
- [119] Lust, K., Roose, D., Spence, A., and Champneys, A. R., “An Adaptive Newton-Picard Algorithm with Subspace Iteration for Computing Periodic Solutions,” *SIAM J. Sci. Comp.*, Vol. 19, 1998, pp. 1188–1209.
- [120] Keller, B. and von Sosen, H., “New Methods in CFD: DAE and RPM,” *Proceedings of the First Asian CFD conference*, Hong Kong, 1995, pp. 17–30.
- [121] Tiesinga, G., *Multi-level ILU preconditioners and continuation methods in fluid dynamics*, Ph.D. thesis, Rijksuniversiteit, Groningen, 2000.
- [122] Love, P., *Bifurcation in Kolmogorov and Taylor-Vortex Flows*, Phd thesis, California Institute of Technology, Pasadena, California, 1999.
- [123] Burrage, K., Erhel, J., Pohl, B., and Williams, A., “A deflation technique for linear systems of equations,” *SIAM J. on Sc. Comp.*, Vol. 19, No. 4, 1998, pp. 1245–1260.
- [124] Burrage, K., Williams, A., Erhel, J., and Pohl, B., “The implementation of a generalized cross validation algorithm using deflation techniques for linear systems,” Report 94-02, Eidgenössische Technische Hochschule, Zürich, 1994.
- [125] Dorobantu, M., Lust, K., Jacobson, C., and Khibnik, A., “The Recursive Projection Method for Acceleration of Iterative Methods,” Tech. rep., United Technologies Research Center, 1999.
- [126] Möller, J., *Aspects of the Recursive Projection Method applied to Flow Calculations*, Ph.D. thesis, Royal Institute of Technology (KTH), Department of Numerical Analysis and Computer Science, Stockholm, Sweden, January 2005.
- [127] Campobasso, M. S. and Giles, M. B., *Computational Fluid Dynamics 2002*, chap. Stabilization of a linear Navier-Stokes solver for turbomachinery aeroelasticity, Springer Verlag, Berlin, Germany, 2003, pp. 343–348.
- [128] Campobasso, M. S. and Giles, M. B., “Stabilization of a linear flow solver for turbomachinery aeroelasticity using Recursive Projection Method,” *AIAA Journal*, Vol. 42, No. 9, 2004, pp. 1765–1774.
- [129] Hsu, J. M. and Jameson, A., “An Implicit-Explicit Hybrid Scheme for Calculating Complex Unsteady Flows,” *AIAA Paper 02-0714*, 2002.
- [130] Hanke, M., “Advanced Numerical Methods,” Lecture Notes, Royal Institute of Technology (KTH), NADA, February 2002.
- [131] Swedish Defence Research Agency (FOI), Aeronautics Div. (FFA), “FFA Matlab Toolbox,” [http://www.edge.foi.se/matlab\\_tools/index.html](http://www.edge.foi.se/matlab_tools/index.html), 2003, accessed 03/2004.
- [132] Möller, J., *Studies of Recursive Projection Methods for Convergence Acceleration of Steady State Calculations*, Licentiate thesis, Royal Institute of Technology (KTH), Dept. of Numerical Analysis and Computer Science, Stockholm, Sweden, 2001, TRITA-NA-0119.

- [133] Anderson, E., Bai, Z., Bischof, C., Blackford, S., Demmel, J., Dongarra, J., Croz, J. D., Greenbaum, A., Hammarling, S., McKenney, A., and Sorensen, D., *LAPACK Users' Guide Third Edition*, SIAM, Philadelphia, 1999, <http://www.netlib.org/lapack/lug/>.
- [134] van de Geijn, R. A., *Using PLAPACK: Parallel Linear Algebra Package*, MIT Press, Cambridge, 1997, <http://www.cs.utexas.edu/users/plapack/Guide/>.
- [135] Blackford, L. S., Choi, J., Cleary, A., D'Azevedo, E., Demmel, J., Dhillon, I., Dongarra, J., Hammarling, S., Henry, G., Petitet, A., Stanley, K., Walker, D., and Whaley, R. C., *ScaLAPACK Users' Guide*, SIAM, Philadelphia, 1997, <http://www.netlib.org/scalapack/slug/>.
- [136] Quintana-Ortí, G., Sun, X., and Bischoff, C. H., "A BLAS-3 version of the QR factorization with column pivoting," *SIAM J. Sci. Comput.*, Vol. 19, 1998, pp. 1486–1494.
- [137] Quintana-Ortí, E., Quintana-Ortí, G., Sun, X., and van de Geijn, R. A., "A note on parallel matrix inversion," *SIAM J. Sci. Comput.*, Vol. 22, 2001, pp. 1762–1771.
- [138] Lane, D. A., "Visualizing Time-Varying Phenomena in Numerical Simulations of Unsteady Flows," *AIAA Paper 96-0048*, 1996.
- [139] (CEI), C. E. I., *EnSight 7 User Manual*, 2002.
- [140] McCormick, B. W., *Aerodynamics, Aeronautics and Flight Mechanics*, 2nd ed., 1995.
- [141] Özgören, M., Sahin, B., and Rockwell, D., "Vortex Structure on a Delta Wing at High Angle of Attack," *AIAA Journal*, Vol. 40, No. 2, February 2002, pp. 285–292.
- [142] Brown, G. L. and Lopez, J. M., "Axisymmetric Vortex Breakdown, Part 2: Physical Mechanisms," *Journal of Fluid Mechanics*, Vol. 221, 1990, pp. 553–576.
- [143] Haimes, R., "pV3: A Distributed System for Large-Scale Unsteady CFD Visualization," *AIAA Paper 94-0321*, 1994.
- [144] Haimes, R. and Edwards, D. E., "Visualization in a Parallel Processing Environment," *AIAA Paper 97-0348*, 1997.
- [145] Haimes, R. and Barth, T., "Application of the pV3 Co-Processing Environment to 3-D Unstructured Mesh Calculations on the IBM SP2 Parallel Computer," *CAS Workshop, NASA Ames*, March 1997.
- [146] Haimes, R., "Visual3: Interactive Unsteady Unstructured 3D Visualization," *AIAA Paper 91-0794*, 1991.
- [147] Oak Ridge National Laboratory, "Parallel Virtual Machine (PVM)," <http://www.csm.ornl.gov/pvm/>, 2004, accessed 11/2004.
- [148] Haimes, R., "pV3 Programmer's Guide, Rev. 2.05," Tech. rep., Massachusetts Institute of Technology, December 2001.
- [149] Haimes, R., "pV3 Server User's Reference Manual, Rev. 2.05," Tech. rep., Massachusetts Institute of Technology, December 2001.
- [150] Haimes, R., "pV3 Batch User's Reference Manual, Rev. 2.05," Tech. rep., Massachusetts Institute of Technology, December 2001.
- [151] Haimes, R. and Kenwright, D., "FX Programmer's Guide," Tech. rep., Massachusetts Institute of Technology, July 2000.
- [152] Reise, F., *Co-processing Visualization of CFD Data Generated in a Distributed and Parallel Computing Environment*, Master's thesis, Royal Institute of Technology (KTH), Department of Aeronautics and Vehicle Engineering, Stockholm, Sweden, February 2004, Skrift 2004-7.
- [153] Munukka, K., "NFFP2-314, WP2: Selection of validation geometry and cases for unsteady turbulent high-alpha computations on a delta wing," Technical Report FAA-98.039, Saab Military Aircraft, Linköping, Sweden, April 1998.
- [154] Soltani, M. R. and Bragg, M. B., "Experimental Measurements on an Oscillating 70-degree Delta Wing in Subsonic Flow," *AIAA Paper 88-2576-CP*, 1988.
- [155] Soltani, M. R. and Bragg, M. B., "Early Vortex Burst on a Delta Wing in Pitch," *AIAA Journal*, Vol. 31, No. 12, December 1993, pp. 2283–2289.

- [156] Tormalm, M., *Numerical Investigation of Vortex Breakdown over a 70 Degree Delta Wing Using an Euler Code*, Master's thesis, Royal Institute of Technology (KTH), Department of Aeronautics, Stockholm, Sweden, 1995, SAAB Report No. L-O-1R158.
- [157] LeMay, S. P., Batill, S. M., and Nelson, R. C., "Leading Edge Vortex Dynamics on a Pitching Delta Wing," *AIAA Paper 88-2559-CP*, 1988.
- [158] Erickson, G. E., "High Angle-of-Attack Aerodynamics," *Annual Review of Fluid Mechanics*, Vol. 27, 1995, pp. 45–88.
- [159] Malmlöf, A., *Investigation of Grid Topology for 70° Swept Delta Wing*, Master's thesis, Royal Institute of Technology (KTH), Department of Aeronautics, Stockholm, Sweden, 2000, Skrift 2000-3.
- [160] Roos, F. and Kegeman, J., "An Experimental Investigation of Sweep-Angle Influence on Delta-Wing Flows," *AIAA Paper 90-0383*, 1990.
- [161] Greenwell, D. I., Defence Evaluation & Research Agency (DERA), private communications, May 2001.
- [162] Barlow, J. B., Rae, W. H., and Pope, A., *Low-Speed Wind Tunnel Testing*, John Wiley & Sons, 3rd ed., 1999.
- [163] Mitchell, A. M., Morton, S. A., Huang, X. Z., and Verhaagen, N. G., "NATO RTO AVT Task Group-080 "Vortex Breakdown over Slender Delta Wings" Validation and Verification, Conclusions and Recommendations," *AIAA Paper 2003-4218*, 2003.
- [164] Mitchell, T., AOARD, Japan, formerly ONERA, private communications, October 2004.
- [165] Lamar, J. E., Obara, C. J., Fisher, B. D., and Fisher, D. F., "Flight, Wind-Tunnel, and Computational Fluid Dynamics Comparison for Cranked Arrow Wing (F-16XL-1) at Subsonic and Transonic Speeds," NASA/TP 2001-210629, NASA, February 2001.
- [166] NASA Langley Research Center, "Homepage for the F-16XL Highlift Project CAWAP," <http://cawap-prism.larc.nasa.gov>, 2002, accessed 12/2004.

## Flow-Field Visualization Videos

Click on an image to start a video.



(a) wmv file



(b) mpg file

Video 1: Time-accurate Euler simulations of the ONERA full-span  $70^\circ$  delta wing ( $\alpha = 27^\circ, 30^\circ, 35^\circ, M_\infty = 0.2$ )

Video 1 visualizes the results of time-accurate Euler simulations of the ONERA full-span  $70^\circ$  delta wing at three different angles of attack and a freestream Mach number of 0.2. At  $\alpha = 27^\circ$  spiral-type vortex breakdown is predicted to occur close to the trailing edge over both sides of the wing. The sense of the spirals is in the opposite direction to the rotational sense of the upstream flow. The spiral structures, however, turn around with respect to time in the sense of the primary vortex. The port and starboard spirals are seen to rotate out of phase. The breakdown location is quasi-steady. An abrupt deceleration of the fluid entrained in the core takes place prior to breakdown. This is compared to a water tunnel visualization of vortex breakdown over a similar geometry. In the following animation, the temporal evolution of the normal force coefficient is related to the upper surface pressure distribution. Regions of low pressure are generated where the helix or spiral comes in proximity to the upper surface in the post-breakdown region. As time progresses these regions of low pressure are seen to move downstream with the progression of the rotating helical structure. This unsteady behavior leads to fluctuations in the aerodynamic coefficients.

At  $\alpha = 30^\circ$  massless particles are injected into the flow field. Upstream of breakdown, the particles form straight streaklines along the vortex core axis. At the point of breakdown, the streaklines kink and start to spiral around the reversed flow region, forming a corkscrew-like distortion of the vortex core. Periodically, disturbances travel upstream. The animation is stopped at an instant in time where the disturbance is at the most upstream chordwise location, revealing that the particles spread almost symmetrically around the reversed flow region at the point of breakdown, resembling bubble-type vortex breakdown. Note also that the transformation from spiral- to bubble-type vortex breakdown is associated with an upstream movement of the breakdown location. The port and starboard breakdown locations are seen to be asymmetric then. This is also observed in the following animation, which show a reversed flow region (blue iso-surface) moving upstream when intermittent bubble-type breakdown occurs over one side of the wing, causing asymmetry and in the port and starboard breakdown location.

Finally, at  $\alpha = 35^\circ$  angle of attack, vortex breakdown is seen to occur close to the apex. The flow entrained in the vortex core is clearly seen to decelerate just upstream of the point of breakdown. The port and starboard breakdown locations are highly asymmetric and fluctuate with time.



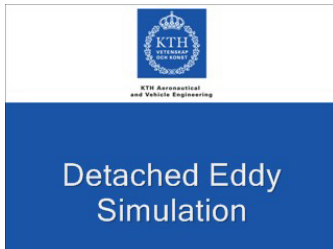
(a) wmv file



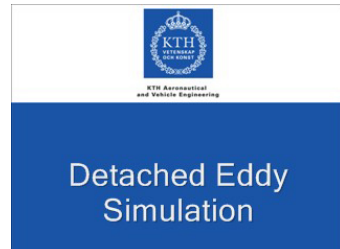
(b) mpg file

Video 2: Time-accurate turbulent simulation of a semi-span  $70^\circ$  delta wing ( $M = 0.16$ ,  $Re = 1.97 \times 10^6$ ,  $\alpha = 35^\circ$ , Spalart-Allmaras one-equation turbulence model)

Video 2 shows the results of a time-accurate fully turbulent simulation (URANS) of a semi-span  $70^\circ$  delta wing at  $\alpha = 35^\circ$ ,  $M_\infty = 0.16$ ,  $Re = 1.97 \times 10^6$ , using the Spalart-Allmaras one-equation turbulence model. The temporal evolution of the normal force coefficient is related to the upper surface pressure distribution and the rotation of the vortex core in the post-breakdown region. Regions of low pressure are generated where the corkscrew-like vortex core comes in proximity to the upper surface. As time progresses these regions of low pressure are seen to move downstream with the progression of the rotating helical structure. This unsteady behavior leads to fluctuations in the aerodynamic coefficients. Also, massless particles are injected into the time-dependent flow field and animated along their pathlines, forming streaklines, which are related to the rotation of the vortex cores. Also note the secondary (and tertiary) vortex cores close to the leading edge.



(a) wmv file



(b) mpg file

Video 3: Detached-eddy simulations of the full-span ONERA  $70^\circ$  delta wing ( $\alpha = 27^\circ$ ,  $M_\infty = 0.2$ ,  $Re = 1.56 \times 10^6$ )

Video 3 shows the results of a grid refinement study for a half-span model of the ONERA  $70^\circ$  delta wing. Solutions were obtained for  $M_\infty = 0.2$ ,  $\alpha = 27^\circ$ , and

$Re = 1.56 \times 10^6$  using DES. The grid was refined in the vortical flow region by increasing the number of grid points of the blocks above the wing by a factor of two in all directions. These refined blocks were connected to the other unrefined blocks using a patched grid boundary condition. The ability of DES to capture the unsteady effects of vortex breakdown is clear. Note that more features are resolved in the post-breakdown region by DES compared to URANS. Also note the secondary vortex close to the leading edge and the structure leaving the wing at the trailing edge. (The patched grid boundary condition is responsible for the vorticity artifacts in the plane through the trailing edge.)



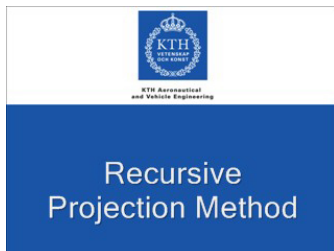
(a) wmv file



(b) mpg file

Video 4: Visualization of steady and unsteady CFD data in a virtual-reality environment

The capabilities of a fully immersive virtual-reality environment for interactive visualization of pre-computed steady and unsteady three-dimensional CFD solutions are demonstrated in Video 4. The first application is the steady airflow around a human female standing in a strong headwind, followed by the steady hypersonic flow around an atmospheric reentry vehicle and the unsteady flow over the full-span ONERA 70° delta wing at high angle of attack.



(a) wmv file



(b) mpg file

Video 5: Fully laminar flow around a circular cylinder ( $M_\infty = 0.1$ ,  $Re = 100$ ) and periodic self-excited turbulent flow around a circular-arc airfoil ( $M_\infty = 0.76$ ,  $Re = 11 \times 10^6$ )

The flow cases shown in Video 5 were computed to evaluate the Recursive Projection Method (RPM) for time-dependent problems. The first sequence shows Mach number

contours computed for the fully laminar time-dependent flow around a circular cylinder at  $M_\infty = 0.1$  and  $Re = 100$ . Vortices are alternately shed from the two shoulders of the cylinder in a regular von Kármán vortex street. The periodic properties of the unsteady flow can clearly be observed in the time history of the lift coefficient,  $C_L$ . After the transients have decayed after about 1.5 s, a periodic solution is obtained. The mean value of the lift coefficient is zero, which is to be expected for a symmetric body in uniform flow. The Strouhal number,  $St$ , with which vortices are shed from the cylinder, can be calculated from the frequency,  $f$ , of the oscillations of the lift coefficient. Here,  $f$  is found to be 5.3759 Hz, corresponding to  $St = 0.1581$ . This is in very good agreement with empirical formulas for an infinitely long circular cylinder.

The second sequence shows results for the periodic self-excited turbulent flow around an 18% thick circular-arc airfoil in free flow at  $M_\infty = 0.76$ ,  $\alpha = 0^\circ$  and  $Re = 11 \times 10^6$ . At these conditions, the transonic flow results in a periodic,  $180^\circ$  out-of-phase motion of the shocks over the upper and lower surface of the airfoil. The unsteadiness is driven by the interaction between the shocks, the boundary layer and the vortex shedding in the wake.

## Appended Papers

### Paper A

S. Görtz, A. Rizzi and K. Munukka, “Computational Study of Vortex Breakdown over Swept Delta Wings,” *AIAA Paper 99-3118*, 1999. [Paper-A.pdf](#)

### Paper B

S. Görtz and A. Rizzi, “Computing the High-Alpha Aerodynamics of Delta Wings - Evaluation and Analysis,” *AIAA Paper 01-0115*, 2001. [Paper-B.pdf](#)

### Paper C

S. Görtz, “Time-accurate Euler Simulations of a Full-Span Delta Wing at High Incidence,” *AIAA Paper 03-4304*, 2003. [Paper-C.pdf](#)

### Paper D

S. Görtz, “Detached-Eddy Simulations of a Full-Span Delta Wing at High Incidence,” *AIAA Paper 03-4216*, 2003. [Paper-D.pdf](#)

### Paper E

S. Görtz and A. Jirásek, “Steady and Unsteady CFD Analysis of the F-16XL-1 at Flight-Reynolds Numbers and Comparison to Flight Test Data,” in *Understanding and Modelling Vortical Flows to Improve the Technology Readiness Level for Military Aircraft*, NATO RTO Technical Report, AVT-113, to appear in 2006. [Paper-E.pdf](#)

### Paper F

S. Görtz and E. Sundström, “Virtual Reality Environment for Visualization of Unsteady Three-Dimensional CFD Data,” *Proceedings ECCOMAS 2004*, 2004. [Paper-F.pdf](#)

### Paper G

S. Görtz and J. Möller, “Recursive Projection Method for Efficient Unsteady CFD Simulations,” *Proceedings ECCOMAS 2004*, 2004. [Paper-G.pdf](#)

### Paper H

S. Görtz and J. Möller, “Evaluations of the Recursive Projection Method for Efficient Turbulent Unsteady CFD Simulations,” *ICAS Paper 2004-2.1.1*, 2004. [Paper-H.pdf](#)

